Title: *C. elegans* DSB-3 Reveals Conservation and Divergence among Protein Complexes Promoting Meiotic Double-Strand Breaks

Authors: Albert W. Hinman[1,2], Hsin-Yi Yeh[3], Baptiste Roelens[1], Kei Yamaya[1], Alexander Woglar[1], Henri-Marc G. Bourbon[4], Peter Chi[3,5], Anne M. Villeneuve[1,2,*]

[1]Department of Genetics, Stanford University School of Medicine, Stanford, California, USA

[2]Department of Developmental Biology, Stanford University School of Medicine, Stanford, California, USA

[3]Institute of Biochemical Sciences, National Taiwan University, Taipei, Taiwan

[4]Centre de Biologie Intégrative (CBI), Molecular, Cellular & Developmental biology unit (MCD), Université Fédérale de Toulouse, Toulouse, France

[5]Institute of Biological Chemistry, Academia Sinica, Taipei, Taiwan

*Correspondence: annev@stanford.edu

Author Contributions:

AH: Designed Research, Performed Research, Analyzed Data, Wrote the Paper

HY: Performed Research, Analyzed Data

BR: Designed Research, Performed Research

KY: Performed Research

AW: Designed Research

HMB: Performed Research, Analyzed Data

PC: Designed Research, Analyzed Data

AV: Designed Research, Analyzed Data, Wrote the Paper

25 **Classification**: Major: Biological Sciences, Minor: Genetics

26

27 **Key Words**: meiosis, *C. elegans,* DNA double-strand breaks, DSB-3, meiotic recombination,

28 Mei4

29

Abstract:

Meiotic recombination plays dual roles in the evolution and stable inheritance of genomes: recombination promotes genetic diversity by reassorting variants, and it establishes temporary connections between pairs of homologous chromosomes that ensure for their future segregation. Meiotic recombination is initiated by generation of double-strand DNA breaks (DSBs) by the conserved topoisomerase-like protein Spo11. Despite strong conservation of Spo11 across eukaryotic kingdoms, auxiliary complexes that interact with Spo11 complexes to promote DSB formation are poorly conserved. Here, we identify DSB-3 as a DSB-promoting protein in the nematode *Caenorhabditis elegans*. Mutants lacking DSB-3 are proficient for homolog pairing and synapsis but fail to form meiotic crossovers. Lack of crossovers in *dsb-3* mutants reflects a requirement for DSB-3 in meiotic DSB formation. DSB-3 concentrates in meiotic nuclei with timing similar to DSB-1 and DSB-2 (predicted homologs of yeast/mammalian Rec114/REC114), and DSB-1, DSB-2, and DSB-3 are interdependent for this localization. Bioinformatics analysis and interactions among the DSB proteins support the identity of DSB-3 as a homolog of MEI4 in conserved DSB-promoting complexes. This identification is reinforced by colocalization of pairwise combinations of DSB-1, DSB-2, and DSB-3 foci in structured illumination microscopy images of spread nuclei. However, unlike yeast Rec114, DSB-1 can interact directly with SPO-11, and in contrast to mouse REC114 and MEI4, DSB-1, DSB-2 and DSB-3 are not concentrated predominantly at meiotic chromosome axes. We speculate that variations in the meiotic program that have co-evolved with distinct reproductive strategies in diverse organisms may contribute to and/or enable diversification of essential components of the meiotic machinery.

55 **Significance Statement**

56 Faithful inheritance of chromosomes during meiosis depends on the formation and repair of
57 double-strand DNA breaks (DSBs), which are generated through the activity of a
58 topoisomerase-like protein known as Spo11. Spo11 exhibits strong conservation throughout
59 eukaryotes, presumably reflecting constraints imposed by its biochemical activity, but auxiliary
60 proteins that collaborate with Spo11 to promote and regulate DSB formation are less well
61 conserved. Here we investigate a cohort of proteins comprising a complex required for meiotic
62 DSB formation in *Caenorhabditis elegans*, providing evidence for both conservation with and
63 divergence from homologous complexes in other organisms. This work highlights the
64 evolutionary malleability of protein complexes that serve essential, yet auxiliary, roles in
65 fundamental biological processes that are central to reproduction.

66

67 **Main Text**

68 **Introduction**

69 Meiotic recombination is important for two reasons. It promotes genetic diversity by
70 reassorting traits, and it is important for creating temporary attachments between pairs of
71 homologous chromosomes that are necessary for their future segregation at the meiosis I
72 division. Recombination is initiated by the programmed introduction of DNA double-strand
73 breaks (DSBs) (1). Some DSBs are repaired by a mechanism that leads to the formation of
74 crossovers (COs) between homolog pairs, and the remaining DSBs are repaired as
75 noncrossover products, thereby restoring genome integrity. Although DSBs are required for CO
76 formation, they may lead to genomic instability if they are not repaired or are repaired
77 erroneously. Thus, DSB formation in meiotic cells is governed by regulatory and surveillance
78 mechanisms that function to ensure that enough DSBs are created to guarantee a CO on each
79 homolog pair while limiting excess DSBs that may endanger the genome (2). Without
80 appropriate DSB formation and repair, COs may fail to form between homologs during meiotic
81 prophase, resulting in unattached homologs (univalents) that mis-segregate during the meiotic
82 divisions, leading to aneuploidy in the resulting progeny.

83 Meiotic DSB formation is catalyzed by Spo11, a topoisomerase-like protein homologous to
84 the catalytic A subunit of archaeal class VI topoisomerases that is well conserved across
85 eukaryotic kingdoms (3–6). The mechanism of DNA breakage involves formation of a covalent
86 linkage between Spo11 protein DNA, analogous to a key intermediate in the topisomerase
87 reaction (1). Despite identification of structural and mechanistic conservation between Spo11
88 and TopVIA more than 20 years ago, however, counterparts of the archaeal TopVIB subunit that
89 partner with Spo11 in “Spo11 core complexes” were not recognized until much later, reflecting
90 substantial divergence both from TopVIB and among their eukaryotic orthologs (7–9).

91 DSB formation also depends on multiple additional factors that play critical roles in
92 determining the location, timing, levels, and regulation of DSB formation (2). Several of these
93 auxiliary DSB-promoting factors, including Rec114, Mei4 and Mer2, were originally discovered
94 through genetic screens in *Saccharomyces cerevisiae* designed to identify genes required for
95 initiation of recombination (10, 11). In contrast to the high level of conservation observed for
96 Spo11, but similar to the other subunits of the Spo11 core complex, many auxiliary DSB protein
97 such Rec114, Mei4 and Mer2 are poorly conserved at the primary sequence level (1). Indeed,
98 high levels of sequence divergence had prevented identification of Rec114, Mei4 and Mer2
99 homologs outside of budding yeast until non-standard bioinformatics approaches were applied
100 (12, 13). Homologs of Rec114 and Mei4 that are required for meiotic recombination have now
101 been identified in several species, including *Mus musculus* (13–15), *Schizosaccharomyces*
102 *pombe* (11, 16, 17), and *Arabidopsis thaliana* (18, 19). Proteins that were independently
103 discovered based on roles in meiotic recombination in the ascomycete *Sordaria macrospora*
104 (Asy1) and in the nematode *Caenorhabditis elegans* (DSB-1 and DSB-2) were also
105 subsequently identified as putative Rec114 homologs (12, 20, 21), but Mei4 homologs were not
106 yet identified in these organisms.
107 Several studies have established that DSB auxiliary factors Rec114 and Mei4 work
108 closely together with each other and with Mer2 to promote meiotic DSB formation. Physical
109 interactions among these proteins and their orthologs have been demonstrated for several
110 organisms (13, 22–26), and coimmunoprecipitation experiments in *M.* musculus have further
111 confirmed that these proteins interact with one another *in vivo* in a meiotic context (15). Recent
112 biochemical analyses have shown that Rec114 and Mei4 together form individual complexes
113 with a stoichiometry of 2 Rec114 molecules for every 1 Mei4 molecule and have further
114 suggested that these complexes may self-assemble into large molecular condensates on
115 chromatin during meiotic progression (27). In both *S. cerevisiae* and *M. musculus,* all three
116 proteins have been reported to localize together in foci on meiotic prophase chromosomes (15,

117 22, 23, 26). Further, mouse REC114 and MEI4 and the Mer2 homolog IHO1 all localize
118 predominantly at the meiotic chromosome axis (15, 26), contributing to the idea that they act as
119 an intermediary between chromosome organization and DSB formation. Consistent with this
120 view, chromatin immunoprecipitation experiments in both *S. cerevisiae* and *S. pombe* have
121 shown that these proteins interact with both axis-enriched DNA sequences and with DSB sites
122 (25, 28–30). Additionally, *S. cerevisiae* Rec114 and Mei4 have been found to interact with the
123 Rec102 and Rec104 subunits that together comprise the TopVIB-like component of the Spo11
124 core complex (9, 23). Together these findings implicate Rec114-Mei4 in recruiting Spo11 to the
125 meiotic chromosome axis.

126 *C. elegans* DSB-1 and DSB-2, while clearly implicated in meiotic DSB formation, were
127 difficult to recognize as Rec114 homologs owing to high sequence divergence (12, 20, 21).
128 Further, *C. elegans* differs from yeast and mice regarding the relationships between DSB
129 formation and meiotic chromosome organization. Whereas DSB-dependent recombination
130 intermediates are required to trigger assembly of the synaptonemal complex (SC) between
131 homologous chromosomes in yeast and mice, *C. elegans* can achieve full synapsis between
132 aligned homologs even in the absence of DSB formation (6). Thus, there are substantial
133 differences in the cellular environments in which DSB-promoting complexes have evolved and
134 function in different organisms.

135 In our current work, we identify DSB-3 as a protein that partners with DSB-1 and DSB-2
136 to promote SPO-11-dependent meiotic DSB formation in *C. elegans*. We demonstrate a
137 requirement for DSB-3 in promoting the DSBs needed for CO formation, and we show that
138 DSB-3 becomes concentrated in germ cell nuclei during the time when DSBs are formed, in a
139 manner that is interdependent with DSB-1 and DSB-2. Through a combination of bioinformatics,
140 interaction data, and colocalization analyses, we identify DSB-3 as a likely Mei4 homolog and
141 establish DSB-1-DSB-2-DSB-3 as functional counterpart of the Rec114-Mei4 complex. Despite
142 homology and a shared role in promoting DSB formation, we uncover surprising differences

143 between the *C. elegans* DSB-1-DSB-2-DSB-3 and the REC114-MEI4 complexes observed in
144 mice, notably that *C. elegans* DSB-1, DSB-2 and DSB-3 are distributed broadly on chromatin
145 rather than becoming concentrated preferentially on chromosome axes. This work highlights the
146 evolutionary malleability of protein complexes that serve essential, yet auxiliary, roles in meiotic
147 recombination. Rapid diversification of such proteins may reflect a relaxation of constraints
148 enabled by changes in another aspect of the reproductive program, or alternatively, they may
149 reflect a capacity of alterations in such proteins to have an immediate impact on reproductive
150 success.

151

152 **Results**

153 **Identification of *dsb-3* as a gene required for the formation of meiotic crossovers**

154 The *dsb-3(me6ts)* allele was isolated in a genetic screen for mutants exhibiting a high
155 incidence of males among the progeny of self-fertilizing hermaphrodites, *i.e.,* the "Him"
156 phenotype, which is indicative of errors in segregation of X chromosomes during meiosis. *me6ts*
157 mutant hermaphrodites exhibit temperature-sensitive meiotic defects affecting both autosomes
158 and X chromosomes (Table 1, Figure 1A). Whereas inviable embryos and males (XO) are rare
159 among the self-progeny of wild-type hermaphrodites (XX), *dsb-3(me6ts)* mutant hermaphrodites
160 raised at the non-permissive temperature of 25°C produce 28% inviable embryos, and 17% of
161 their surviving progeny are males. Further, DAPI staining of chromosomes in oocytes at
162 diakinesis, the last stage of meiotic prophase, revealed a defect in chiasma formation in the
163 *dsb-3(me6ts)* mutant, reflecting an underlying defect in crossover formation (see below).
164 Whereas wild-type oocyte nuclei consistently exhibit 6 pairs of homologous chromosomes
165 connected by chiasmata (bivalents), oocyte nuclei in the *dsb-3(me6ts)* mutant exhibited a

166 mixture of bivalents and unattached (achiasmate) chromosomes (univalents), with the incidence
167 of univalents increasing with time.

168 Mapping and sequencing identified a missense mutation at genomic position IV:
169 7758710 (WS279) as the likely causal mutation responsible for the *dsb-3(me6ts)* mutant
170 phenotype (see Materials and Methods); this mutation results in a Leu165Phe substitution in the
171 previously uncharacterized protein C46A5.5. CRISPR/Cas9 genome editing was used to
172 introduce multiple stop codons early into the first exon of *C46A5.5*, thereby creating the null
173 allele *me115* (Figure 1B). *me115* fails to complement *dsb-3(me6ts)* (Figure 1A), confirming the
174 identity of *C46A5.5* as *dsb-3*.

175 Analysis of the *dsb-3(me115)* null mutant indicates that the DSB-3 protein is required for
176 the formation of meiotic crossovers between all six pairs of homologous chromosomes. *dsb-*
177 *3(me115)* mutant hermaphrodites produced 99% inviable embryos, and 25% of their surviving
178 progeny were male, reflecting mis-segregation of autosomes and X chromosomes (Table 1).
179 Diakinesis oocytes of *dsb-3(me115)* mutant hermaphrodites exhibited an average of 11.6 ± 0.6
180 DAPI-stained bodies, indicating of a lack of chiasmata connecting all six homolog pairs (Figure
181 1A). A severe defect in crossover formation in the *dsb-3(me115)* mutant was also revealed
182 using GFP::COSA-1 as a cytological marker of crossover-designated sites in late pachytene
183 nuclei ((31); Figure 1C). Whereas 6 GFP::COSA-1 foci (1 per homolog pair) were consistently
184 observed in late pachytene nuclei of control worms, GFP::COSA-1 foci were absent from most
185 late pachytene nuclei in the *dsb-3(me115)* mutant.

186 Since pairing and assembly of the synaptonemal complex between homologous
187 chromosomes are prerequisites for the formation of crossovers during *C. elegans* meiosis, we
188 evaluated whether these features were impaired in the *dsb-3(me115)* mutant. We assessed
189 pairing using fluorescence *in-situ* hybridization (FISH) for a 1 Mbp segment of Chromosome II
190 and immunostaining for HIM-8, a C2H2 zinc-finger DNA-binding protein that concentrates on the

191 Chromosome X pairing center (32, 33), demonstrating that *dsb-3(me115)* mutants are proficient
192 for homolog paring (Figure 1D). Further, immunostaining for the axial element protein HTP-3
193 and the synaptonemal complex central region protein SYP-2 (34, 35) revealed fully synapsed
194 chromosomes in early pachytene nuclei in the *dsb-3(me115)* mutant, indicating successful SC
195 assembly (Figure 1E). Together these data indicate that the DSB-3 protein is dispensable for
196 pairing and synapsis, and point to a role for this protein in the DNA events of recombination.

197 During *C. elegans* meiosis, failure to form crossover recombination intermediates
198 between one or more chromosome pairs prolongs the early pachytene stage of meiotic
199 prophase, reflecting the operation of a "crossover assurance" checkpoint (20, 21, 36).
200 Consistent with the observed deficit of interhomolog crossovers, *dsb-3(me115)* mutant gonads
201 display an extended zone of nuclei exhibiting phosphorylation of nuclear envelope protein SUN-
202 1, a marker of crossover assurance checkpoint activation (Supplemental Figure 1A).

203 **DSB-3 is required for meiotic double-strand break formation**

204 Meiotic recombination is initiated through the formation of DSBs by the conserved
205 topoisomerase-like protein SPO-11 (3, 6). Following formation, these DSBs are then processed
206 to enable the loading of the DNA strand-exchange protein RAD-51 (37, 38). RAD-51 foci thus
207 mark the sites of recombination intermediates that can be assayed as a proxy for successful
208 initiation of meiotic recombination (35, 39). We observed a strong decrease in the number of
209 RAD-51 foci in *dsb-3(me115)* mutants relative to wild type (Figure 2A), suggesting that fewer
210 DSBs are being created in these mutants or that there is a failure to load RAD-51 at DSB sites.

211 To determine whether fewer endogenous DSBs was the defect responsible for the observed
212 reduction in RAD-51 foci, we used γ-irradiation to introduce ectopic DSBs to test whether such
213 breaks are sufficient to restore crossover formation. Similar approaches were taken with other
214 DSB-defective mutants in *C. elegans,* such as *dsb-1*, *dsb-2*, and *spo-11* (6, 20, 21). Young adult

215 *dsb-3(me115)* and *dsb-3(me6ts)* hermaphrodites (alongside wild-type and *spo-11(me44)*
216 controls) were exposed to 5000 rad of γ-irradiation and subsequently assayed for crossover
217 formation through DAPI staining of chromosomes in oocyte nuclei. We observed a full rescue of
218 normal DAPI-body counts after irradiation (Figure 2B), suggesting that the *dsb-3* mutants are
219 specifically defective in DSB formation.

220 **DSB-3 is concentrated in DSB-competent nuclei and is interdependent with DSB-1 and**
221 **DSB-2**

222 Consistent with its role in promoting meiotic DSB formation, we find that DSB-3 localizes to
223 germ cell nuclei during the time when meiotic DSBs are formed. To assess DSB-3 localization in
224 the germ line, we generated a transgenic strain that expresses a DSB-3::GFP fusion protein in
225 the germ line in the *dsb-3(me15)* null mutant background (*meSi7[sun-1p::dsb-*
226 *3::gfp::sun13'UTR]* II; *dsb-3(me115)* IV); based on assessment of progeny viability and DAPI
227 bodies in diakinesis oocytes, we infer that this DSB-3::GFP fusion protein is largely functional in
228 promoting meiotic recombination (Table 1). Immunolocalization experiments in whole-mount
229 dissected gonads show that DSB-3::GFP becomes concentrated in germ cell nuclei within the
230 transition zone, soon after entry into meiotic prophase (Figure 3A). The DSB-3::GFP
231 immunofluorescence signal is strongest in early pachytene nuclei, then declines sharply in mid-
232 pachytene, albeit with a few outlier nuclei in the late pachytene region of the gonad retaining a
233 strong DSB-3 signal. This pattern of appearance and disappearance of DSB-3 from germ cell
234 nuclei is similar to the patterns observed for the double-strand break promoting proteins DSB-1
235 and DSB-2 ((20, 21) and Figure 3A), and corresponds to the timing when nuclei are competent
236 for meiotic DSB formation.

237 The DSB-3, DSB-2, and DSB-1 proteins are not only abundant in the same nuclei during
238 early meiotic prophase, but they are also interdependent for this immunolocalization. Previous
239 studies had demonstrated interdependence for DSB-1 and DSB-2 (20, 21), with loss of the

240 DSB-2 immunofluorescence signal in a *dsb-1* null mutant (which lacks meiotic DSB-promoting
241 activity) and reduction of DSB-1 immunofluorescence signal in a *dsb-2* null mutant (which
242 retains a low residual level of DSB-promoting activity). Similarly, we found that DSB-3::GFP
243 immunofluorescence signal was abolished in *dsb-1* null mutant germ lines (Figure 3B).
244 Likewise, DSB-3::GFP immunofluorescence signal was reduced in *dsb-2* null mutant germ lines
245 and was restricted to a few rows of nuclei in the transition zone and very early pachytene
246 regions of the gonad (Figure 3B). Conversely, DSB-1 and DSB-2 immunostaining were lost in
247 *dsb-3(me115)* mutant germ lines (Figure 3C). Collectively, these data indicate that DSB-3, DSB-
248 2, and DSB-1 are interdependent for proper localization to germ cell nuclei, indicating that they
249 function together in promoting meiotic DSB formation.

250 Together, our data demonstrating 1) a similar requirement in promoting DSB formation, 2)
251 concentration in the same nuclei, and 3) interdependence for localization and/or abundance in
252 meiotic nuclei are all consistent with DSB-3 functioning in a protein complex together with DSB-
253 1 and DSB-2 to promote the formation of SPO-11-dependent meiotic DSBs.

254 **Evidence that DSB-1, DSB-2 and DSB-3 form a complex homologous to the yeast and**
255 **mammalian Rec114-Mei4 complexes**

256 Although the initial PSI-BLAST searches conducted for DSB-1 and DSB-2 had not
257 identified homologs outside of *Caenorhabditis* (20, 21), DSB-1 and DSB-2 were subsequently
258 identified as likely distant homologs of the Rec114 meiotic DSB-promoting proteins from fungi
259 and mammals (12). This identification was enabled using an approach involving PSI-BLAST
260 searches initiated using sequence alignments, in combination with scanning for patterns of
261 similarity in predicted secondary structure, to identify short signature motifs (SSMs) in poorly
262 conserved proteins (40). We obtained additional support for the assignment of DSB-1 and DSB-
263 2 as Rec114 homologs using the Phyre2 structure prediction server (41), which identified
264 medium confidence (#6 hit, 40.3%) and low confidence (#19 hit, 11.9%) alignments between the

265 N-terminal domains of DSB-2 and DSB-1 and the N-terminal domain (where the identified SSMs
266 are located) of the solved structure of mouse Rec114 (42). We therefore used an alignment
267 driven PSI-BLAST approach similar to that described above to identify DSB-3 as a putative
268 homolog of Mei4 (see Materials and Methods, Figure 4A, Supplemental Figure 2), which is
269 required for meiotic DSB formation in yeast and mice and forms a complex with Rec114 (13–15,
270 22, 24, 43). Based on local amino acid composition and relative position in the protein
271 sequence, three of the 6 SSMs previously identified in Mei4 homologs from diverse species
272 (SSMs #1, 4 and 6) are well supported in the *Caenorhabditis* DSB-3 orthologs, while the other
273 three SSM are less well conserved.

274 To complement these *in silico* analyses, we used yeast two-hybrid (Y2H) assays to establish a
275 network of interactions among the DSB-1, DSB-2, and DSB-3 proteins and SPO-11, the protein
276 that catalyzes DSB formation (Figure 4B, Supplemental Figure 2). Y2H interactions were
277 detected between DSB-1 and DSB-2 and between DSB-1 and DSB-3, consistent with an ability
278 of these proteins to form complexes. Homotypic interactions were also detected both for DSB-1
279 and for DSB-2. In addition to the interactions detected among the putative Rec114 and Mei4
280 homologs, DSB-1 also interacted with SPO-11 in the Y2H assay.

281 We note that a truncated version of DSB-1 lacking the N-terminal 33 amino acids loses the
282 ability to interact with SPO-11 but retains its ability to associate with DSB-2 and DSB-3. This
283 suggests that the interactions between DSB-1 and SPO-11 and the interactions between DSB-1
284 and DSB-2 or DSB-3 may be mediated, at least in part, by different parts of the DSB-1 protein.

285

286 **DSB-3, DSB-2, and DSB-1 colocalize in meiotic nuclei**

287 To complement our genetic, bioinformatic, and Y2H evidence that DSB-3, DSB-2, and
288 DSB-1 function together as components of conserved protein complexes to promote DSB

289 formation, we investigated their colocalization using Structured Illumination Microscopy (SIM) on
290 spread preparations of meiotic nuclei (Figure 5). For most of these analyses, we used a
291 moderate nuclear spreading protocol (44), coupled with SIM imaging to provide improved spatial
292 resolution below the limits of standard light microscopy (45). This approach enabled detection of
293 these proteins as chromosome-associated foci. To facilitate co-staining of protein pairs for these
294 colocalization analyses, we used CRISPR/Cas9 gene editing to create strains expressing HA or
295 FLAG tagged versions of the DSB proteins from the endogenous loci (Table 1), and we
296 detected the proteins using indirect immunofluorescence.

297 We used the image analysis pipeline outlined in Figure 5A (described in more detail in
298 Supplemental Figure 3) to identify DSB protein foci and to conduct object-based colocalization
299 analyses to assess the degree of colocalization detected for pairwise combinations of the
300 imaged DSB proteins within individual nuclei. As negative controls, we generated virtual nuclei
301 in which the second channel in each combination was rotated by 90° in XY, resulting in virtual
302 composite images in which DSB protein foci are modified in location, but numbers, sizes, and
303 intensity distributions of foci remain unaltered. Collectively, our analyses indicate that the DSB-
304 3, DSB-2, and DSB-1 proteins strongly colocalize with each other in meiotic prophase nuclei.

305 Analysis of all three pairwise combinations of DSB-1, DSB-2, and DSB-3 foci are
306 presented in Figure 5B-D and Supplemental Figure 4. For all three pairs, numbers of foci for the
307 two channels detected in each nucleus were strongly correlated, consistent with expectations
308 for components of the same protein complex. Further, substantial colocalization was observed
309 for each pair. For example, we found that 45 ± 5% of DSB-2 foci colocalized with DSB-3::GFP
310 foci, and conversely, that 37 ± 7% of DSB-3::GFP foci colocalized with DSB-2 foci. In contrast,
311 negative control coincidental colocalization values were 10 ± 3% and 8 ± 3%, respectively.
312 Similarly, 52 ± 8% of 3xFLAG::DSB-3 foci colocalized with 3xHA::DSB-1 foci, and conversely
313 55% ± 5% of 3xHA::DSB-1 foci colocalized with 3xFLAG::DSB-3 foci. Likewise, 43 ± 11% of

314 3xHA::DSB-1 foci colocalized with DSB-2 foci, and conversely 41 ± 9% of DSB-2 foci
315 colocalized with 3xHA::DSB-1 foci.

316 Although substantial colocalization was observed for all pairwise combination of DSB-1,
317 DSB-2 and DSB-3 foci, the fraction of colocalization may seem lower than might be anticipated
318 for proteins comprising the same protein complex. We note, however, that incomplete
319 colocalization has been similarly observed for the Rec114 and Mei4 proteins in both budding
320 yeast and mouse meiocytes (22, 26). One possible explanation is that only a subset of these
321 protein molecules occur together in complexes, while other molecules exist separately within the
322 nucleus; however, this explanation is not easily reconciled with the observed interdependence
323 among these proteins. Another possibility is that the observed degree of colocalization reflects
324 limitations on our ability to detect all of the DSB-1, DSB-2 and DSB-3 target molecules that are
325 present. *e.g.* because of isoforms that lack epitopes or because the complexes and/or their
326 components may be organized in a manner that makes some epitopes inaccessible to detection
327 reagents.

328 This latter possibility is supported by data from an experiment in which we assessed
329 colocalization for fluorescent foci representing separate epitopes on the same protein,
330 3xHA::DSB-2, expressed from the endogenous *dsb-2* locus. Specifically, we used a mouse
331 monoclonal antibody (mAB) against the HA epitope and rabbit polyclonal (pAB) antibodies
332 raised against the C-terminal 100 amino acids of the DSB-2 protein. The numbers of foci for the
333 two channels detected in each nucleus were strongly correlated (Figure 5C), as expected for
334 foci representing the same target molecule. However, colocalization was again incomplete, in
335 both directions: 44 ± 5% of DSB-2 pAB foci colocalized with HA mAB foci, and conversely, 48 ±
336 2% of HA mAB foci colocalized with DSB-2 pAB foci. This incomplete colocalization of HA mAB
337 and DSB-2 pAB fluorescent signals supports the conclusion that a subset of epitopes on DSB-2
338 proteins present in the nucleus were not detected in these experiments.

339 For the DSB-2 - DSB-3::GFP combination, we also conducted a colocalization analysis
340 on “super-spread” nuclei, in which chromosomes were dispersed over an area 6-10 times larger
341 than that of an unperturbed nucleus (46) (Materials and Methods and Supplemental Figure S5).
342 The numbers of foci detected using this approach were 3-5 times higher than the numbers
343 observed in our analysis of partial spreads, but a similar degree of colocalization was detected:
344 55 ± 16% of DSB-2 foci colocalized with DSB-3::GFP foci, and conversely, 44 ± 10% of DSB-
345 3::GFP foci colocalized with DSB-2 foci. The observation of larger numbers of foci with a
346 comparable degree of colocalization suggests the possibility that groups of DSB protein
347 complexes may be split into smaller cohorts by the super-spread procedure.

348

349 **The Presence and Colocalization of DSB-3, DSB-2, and DSB-1 Is Not Confined to the**
350 **Meiotic Chromosomal Axis**

351 Previous chromatin immunoprecipitation experiments in *S. cerevisiae* have shown that
352 Mei4 and Rec114 are enriched at DNA sequences that are also enriched for meiosis-specific
353 axis proteins Hop1 and Red1 (28, 30). Moreover, *M. musculus* Mei4 and Rec114 were found to
354 colocalize cytologically on the axes of meiotic prophase chromosomes (14, 15, 26). Based on
355 these observations, it has been proposed that the Rec114-Mei4 complex primarily functions at
356 the chromosome axes. Strikingly, DSB-1, DSB-2, and DSB-3 foci are not enriched at the
357 chromosome axis during *C. elegans* meiosis. Rather, we find that most foci are detected away
358 from the axis, in the associated chromatin loops (Figure 6A). To quantify axis association, we
359 first segmented images by creating axis masks for each nucleus that corresponded to the pixels
360 containing the immunofluorescence signal derived from the axis protein HTP-3 (Supplemental
361 Figure 3B), then for each DSB protein tested, we identified the subset of foci, termed “axis-
362 associated foci” for which some or all of the pixels coincided with the axis mask. This approach
363 indicated that only 15-30% of DSB protein foci detected in our analyses overlapped with

364 chromosome axis signal, indicating that on spread chromosomes from meiotic nuclei. the
365 preponderance of DSB protein foci detected were not associated with the meiotic chromosome
366 axes.

367 We also assessed whether DSB protein foci associated with the chromosome axis might
368 exhibit a higher degree of colocalization with their DSB protein partners relative to the level of
369 colocalization observed for the full set of foci within the nucleus (Figure 6B). However, this
370 analysis did not reveal any consistent enrichment of colocalization for DSB protein foci that were
371 linked to the chromosome axis. Thus, while components of the meiotic chromosome axis do
372 have roles in promoting and regulating SPO-11 dependent DSB forming activity in *C. elegans*
373 meiosis(47–49), these roles do not appear to be mediated by concentrating DSB-1-DSB-2-DSB-
374 3 complexes in close proximity to the chromosome axis.

375

376 **Discussion**

377 Initiation of meiotic recombination by programmed DSB formation is an ancient and
378 conserved feature of the meiotic program that predates divergence of plants, animals and fungi.
379 Thus, it is not surprising that Spo11, the protein directly responsible for catalyzing DSB
380 formation, is strongly conserved across kingdoms, given constraints imposed by its requirement
381 to interact with and perform chemistry on DNA. However, many additional proteins required for
382 DSB formation had been identified in the yeast system, but plant and metazoan homologs of
383 these auxiliary DSB proteins had long eluded detection by standard BLAST analyses. The
384 barrier to detection of homologs outside fungi was eventually breached using secondary
385 structure prediction coupled to MAFFT alignment and phylogenomically-oriented PSI-BLAST
386 searches (13), which identified characteristic SSMs for putative Mei4 and Rec114 homologs;

387 moreover, the veracity of these predictions was borne out by demonstration of meiotic roles in
388 mouse mutants (13–15).

389 Auxiliary proteins involved in DSB formation during *C. elegans* meiosis were identified
390 independently based on analysis of meiotic mutants ((20, 21), this work). However, recognition
391 of these proteins as distant homologs of conserved DSB-promoting factors came later, after
392 their functional importance in DSB formation was already established (12). Identification of DSB-
393 1 and DSB-2 as Rec114 homologs was further solidified by alignments of the predicted
394 structure of DSB-1 and DSB-2 with the solved structure of mouse REC114 ((42); this work).
395 Likewise, our initial identification of *C. elegans* DSB-3 as a factor important for meiotic DSB
396 formation was similarly based on functional data. The identity of DSB-3 as a putative Mei4/MEI4
397 ortholog was derived computationally from alignments and collinearity of SSMs among
398 metazoan homologs, and this identification was reinforced by demonstration of Y2H
399 interactions, colocalization and interdependence with Rec114 homologs DSB-1 and DSB-2.
400 Thus, despite a high degree of divergence at the amino acid sequence level, our data
401 collectively support the conclusion that DSB-1, DSB-2 and DSB-3 together form complexes that
402 are the functional counterpart of Rec114-Mei4 complexes.

403 Having established conservation among the auxiliary complexes that promote the DSB-
404 forming activity of Spo11, our analyses also reveal interesting differences. First, whereas yeast
405 and mice each have only a single Rec114/REC114 ortholog, nematodes in the Caenorhabditis
406 genus each have 2 paralogs, indicating duplication and divergence in the parental lineage.
407 DSB-1 and DSB-2 are neither identical to nor functionally interchangeable with each other, as
408 DSB formation is strongly reduced in *dsb-2* mutants and eliminated in *dsb-1* mutants.
409 Interestingly, recent biochemical analyses indicate a 2 Rec114 : 1 Mei4 stoichiometry of the
410 yeast complex (27). The interdependence of DSB-1 and DSB-2 for nuclear enrichment, in
411 combination with the colocalization observed in chromosome spreads (this work) suggest that

412 the *C. elegans* complexes may typically contain one DSB-1 subunit and one DSB-2 subunit
413 (rather than two identical subunits). However, there is low residual DSB-promoting activity
414 present in *dsb-2* null mutants, suggesting that complexes with two DSB-1 subunits may form
415 and be partially functional when DSB-2 is absent. While the data do support functional
416 diversification of the *C. elegans* Rec114 paralogs, however, how this diversification came about
417 and/or how and why it persisted remain unknown.

418 A second apparent distinction between *C. elegans* DSB-1, DSB-2 and DSB-3 and their
419 mouse counterparts is the observed relationship to meiotic chromosome axes. Mouse REC114
420 and MEI4 are reported to localize predominantly at chromosome axes in spread preparations of
421 meiotic prophase chromosomes, in a manner mediated by Mer2 homolog IHO1 (15, 26) . This
422 association with chromosome axes led to the proposal that a major role for the Rec114 – Mei4
423 complex is to recruit the Spo11 core complex to the axis to activate its DSB-promoting activity
424 specifically in close proximity to the axis, where DSB repair predominantly occurs. In *C.*
425 *elegans*, meiosis specific HORMAD proteins HTP-1 and HTP-3, which are major building blocks
426 of the chromosome axis, are implicated in playing important roles in promoting and regulating
427 meiotic DSB formation (47–49). HTP-3 is strictly required for DSB formation, and HTP-1 is
428 required for normal levels of DSB activity. However, despite this requirement for axis
429 components in DSB formation, our analysis here indicates that DSB-1-DSB-2-DSB-3 complexes
430 are not preferentially enriched adjacent to axes. This may reflect lack of an apparent
431 *Caenorhabditis* ortholog of IHO1, which is recruited to mouse meiotic chromosomes through a
432 direct interaction with HORMAD1.

433 Given the observed lack of enrichment of DSB-1, DSB-2 and DSB-3 at the axes, the
434 role(s) of *C. elegans* meiotic HORMAD proteins in promoting DSB formation may not be strictly
435 limited to recruiting the homologs of Rec114 and Mei4 to chromosomes. One possibility is that
436 the *C. elegans* HORMADs might be involved in activating the subset of DSB-1-DSB-2-DSB-3

437 complexes that do occur in close proximity to the axis. Alternatively, the role(s) of the *C. elegans*
438 axis proteins might be indirect, *e.g.* assembly of the axis might potentially signal successful
439 formation of chromosome structure that is proficient for meiotic DSB repair, thereby licensing
440 the nucleus that it is safe to proceed with DSB formation. The possibility of this signaling
441 scenario is strengthened by prior work demonstrating a role for *C. elegans* HORMAD proteins in
442 a signaling process that sustains activity of protein kinase CHK-2, a master regulator of multiple
443 processes during meiosis, including nuclear enrichment of DSB-1 and DSB-2 (20, 21, 36, 50).

444 It is possible that the observed difference between mice and *C. elegans* regarding axis
445 enrichment of Rec114-Mei4 complexes may be related to differences in spatial organization of
446 recombination events in the genome and/or in coupling between DSB repair and homolog
447 recognition. Meiotic recombination in mice occurs predominantly within 1-2 kb “hotspot’ regions,
448 separated by larger (50-100kb) cold regions where the probability of recombination is very low.
449 A similar “local hotspot” distribution of recombination events was not observed in *C. elegans* (for
450 the portion of the genome studied) (51, 52), suggesting that different constraints are operating
451 to dictate where DSBs may form. Further, there is substantial variation among organisms
452 regarding their relative dependence on different mechanisms that promote pairwise alignment
453 and synapsis between homologous chromosomes. In mouse meiosis, formation of early
454 SPO11-dependent DSB repair intermediates appears to be the main mechanism of homology
455 verification, required to trigger SC assembly and constraining it to occur strictly between aligned
456 homologous chromosomes (53, 54). In contrast, in *C. elegans*, local *cis*-acting chromosomal
457 domains known as pairing centers play a primary role in homolog recognition, and these are
458 capable of promoting largely successful pairwise synapsis between homologs even in the
459 absence of recombination (55). We speculate that differences in the constraints governing the
460 genomic locations of DSBs and/or differences in dependence on DSBs for homology verification
461 may have either contributed to, or been enabled by, diversification of meiotic DSB auxiliary

462 protein complexes. We note that high divergence among essential components of key biological
463 processes is a hallmark not only of the meiotic program, but of reproduction more generally (1,
464 56, 57). This likely reflects multiple underlying factors, including the potential for changes in
465 such proteins to have an immediate impact on processes that directly affect fitness by
466 modulating reproductive success.

467 A key question regarding the role(s) of the Rec114-Mei4 (or DSB-1-DSB-2-DSB-3)
468 complexes is how exactly they are functioning to promote Spo11 activity. It was recently
469 proposed that Rec114-Mei4 complexes function by forming large DNA-dependent biomolecular
470 condensates that promote DSB activity by causing a high local concentration of Spo11 core
471 complexes at presumptive DSB sites held adjacent to the chromosome axis (27). This model
472 was proposed based on: 1) a large segment of the Rec114 protein exhibiting a high probability
473 of disorder, 2) the ability of purified Rec114-Mei4 complexes to promote formation of DNA-
474 dependent condensates *in vitro*, and 3) an ability of Rec114-Mei4 complexes to interact with
475 and recruit the Spo11 core complex. While evaluating potential for *in vitro* condensation is
476 outside the scope of the current study, we note that some of the above attributes may be shared
477 with the *C. elegans* DSB-1-DSB-2-DSB-3 complex. First, based on the Y2H data, the DSB-1-
478 DSB-2-DSB-3 complex is expected to be able to interact with SPO-11 complexes. However, in
479 yeast, interactions occur between Rec114 and the Rec102 and Rec104 components (which
480 together correspond to Top6BL) of the Spo11 core complex, whereas in *C. elegans,* a Top6BL
481 homolog has not yet been identified, and DSB-1 can interact directly with SPO-11 itself in the
482 Y2H assay. Second, the DSB-1 and DSB-2 proteins have long segments with predicted protein
483 disorder scores that hover around 0.5 and include short segments scoring >0.5, leaving it
484 ambiguous whether these might represent *bona fide* disordered regions. Third, the observation
485 that higher numbers of DSB-2 and DSB-3 foci are detected in super-spread nuclei than in
486 moderately-spread nuclei raises the possibility that these proteins might normally occur in larger

487 groups within intact nuclei, potentially analogous to the condensates proposed to occur during
488 yeast meiosis. In either system, future investigations aiming to test predictions of the
489 condensation model will need to address the challenge of visualizing complex dynamic behavior
490 *in vivo*.

491

492 **Materials and Methods**

493 <u>*C. elegans* strains</u>

494 Strains were cultured at 20℃ using standard nematode growth conditions (58) unless
495 otherwise noted. Strains used in this study:

496

497 AV28 *dsb-3(me6ts)* IV
498 AV776 *spo-11(me44) IV / nT1[qIs51]* (IV;V)
499 AV818 *meIs8[gfp::cosa-1]* II; *cosa-1(tm3298)* III
500 AV913 *dsb-3(me6ts)* IV
501 AV958 *dsb-3(me6ts) dpy-20(e1282)* IV
502 AV994 *dpy-3(e184) dsb-3(me6ts)* IV
503 AV995 *dsb-3(me115) IV / nT1 (*IV;V)
504 * AV1029 *meSi7* [*sun1p::dsb-3::gfp::sun-1 3'UTR] II; dsb-3(me115) IV*
505 AV1045 *meSi7 II; dsb-3(me115) dsb-1(we11) / nT1 IV*
506 AV1081 *meSi7 dsb-2(me96) / mnC1 II; dsb-3(me115) IV*
507 AV1095 *dsb-3(me115) / tmC5 [F36H1.3(tmIs1220)]* IV
508 ^ AV1102 *dsb-1(me124[3xha::dsb-1]) dsb-3(me125[3xflag::dsb-3]) IV*
509 ^ AV1115 *dsb-2(me132)[3xha::dsb-2] II*
510 AV1132 *meIs8[gfp::cosa-1]* II*; cosa-1(tm3298)* III*; dsb-3(me115)* IV */ nT1* (IV;V)

511 Bristol N2 Wild type

512 * The transgene allowing expression of the DSB-3::GFP fusion protein was obtained using the
513 Mos Single Copy Insertion strategy (MosSCI, (59)) using the *ttTi5605* insertion on chromosome
514 II as a landing site. The donor plasmid, pBR253, was obtained by assembling fragments
515 carrying the upstream promoter region of the *sun-1* gene, the *sun-1* downstream 3'UTR region,
516 and the genomic sequence of *dsb-3* (coding exons and introns), together with a DNA fragment
517 containing a version of GFP optimized for germline expression (60), into pBR49, a derivative of
518 pCFJ350 modified to enable type IIs restriction/ligation cloning (61). The genomic fragments
519 were obtained by PCR amplification of wild-type genomic DNA using the following primer pairs.
520 The primers for the *sun-1* promoter were oBR840
521 (cgtcgatgcacaatccGGTCTCaCCTGatttccagatttcatcgtcggtttt) and oBR841
522 (agtggaatgtcagGGTCTCaCATaccgagtagatctggaagtttag). The primers for *dsb-3* CDS were:
523 oBR836 (cgtcgatgcacaatccGGTCTCaTATGATCGAAATTACCGATGATGAGG)
524 and oBR837 (agtggaatgtcagGGTCTCaCTCCATTGCTATATCTCTGTTGATTATCTAAAAAC)
525 The primers for the *sun-1* 3'UTR were oBR842
526 (cgtcgatgcacaatccGGTCTCaTAAAaaacgccgtattattgttcctgc) and oBR843
527 (agtggaatgtcagGGTCTCaGTCAttagtaagttaaagctaaagttagcag). The GFP fragment was obtained
528 by PCR amplification of pCFJ1848 (60), using oBR406
529 (cgatgcacaatccGGTCTCaGGAGGTGGATCATCCTCCACATCATCCT) and oBR407
530 (agtggaatgtcagGGTCTCaTTTATGGGGAAGTACCGGATGACG). Correct assembly of all
531 fragments within the donor plasmids was verified by sequencing.

532 ^ In order to perform pairwise colocalization experiments between DSB-1, DSB-2 and DSB-3,
533 we created strains expressing endogenously-tagged versions of these proteins so each pair
534 could be detected using compatible primary antibodies generated in different host organisms.
535 For these strains, we used direct injection of Cas9 protein (PNAbio) complexed with single-

536 guide RNA (sgRNA) (Dharmacon) using the protocol of (62). CRISPR targeting (crRNA)
537 sequences were designed using Benchling (https:// benchling.com/). Small single-stranded
538 oligonucleotides (< 200 bp) were purchased (Integrated DNA Technologies) and used as the
539 repair templates to generate the various tags and nonsense alleles. N2 worms (P0) were
540 injected with the mix together with sgRNA and repair template for the *dpy-10* co-CRISPR
541 marker (63). Rol F1s (carrying *dpy-10(Rol)* marker) were singled out, and a subset of F2
542 progeny was fixed and stained with DAPI (see below) to assess the phenotype of diakinesis
543 nuclei for null alleles. From plates containing worms exhibiting univalents at diakinesis, the new
544 mutations were recovered from siblings of the imaged worms and balanced by *nT1* IV or *tmc5*
545 IV. Tagged alleles were confirmed by immunofluorescence staining (see below). All edits were
546 confirmed by Sanger sequencing of PCR fragments amplified using primers designed to detect
547 the edit event. The crRNAs used, description of the edits, and PCR sequencing primers used
548 are included in Supplemental Table 1.

549 Isolation, mapping, and genomic identification of the *dsb-3(me6ts)* mutation

550 *dsb-3(me6ts)* was isolated in a genetic screen for meiotic mutants exhibiting a high incidence of
551 males as described in (64). After backcrossing (four times) to generate the AV913 strain,
552 homozygous *me6ts* worms were subjected to whole-genome sequencing. DNA was extracted
553 from ~8 60mm confluent plates of N2 and AV913 gravid adult worms; worms were rinsed twice
554 in M9 and resuspended in 10 mM EDTA and 0.1 M NaCl. Worms were then: pelleted; flash
555 frozen in liquid nitrogen; resuspended in 450 µL of lysis buffer containing 0.1 M Tris, pH 8.5, 0.1
556 M NaCl, 50 mM EDTA, and 1% SDS plus 40 µL of 10 mg/mL proteinase K in TE (10 mM Tris, 1
557 mM EDTA), pH 7.4; vortexed; and incubated at 62°C for 45 min. Two successive phenol-
558 chloroform extractions were performed using the Phase Lock gel tubes from Invitrogen, and
559 DNA was precipitated with 1 mL of 100% ethanol plus 40 µL of saturated NH_4Ac (5 M) and 1 µL
560 of 20 mg/mL GlycoBlue. The DNA pellet was washed with 70% ethanol, air dried, and

561 resuspended in 50 µL of TE, pH 7.4. Paired end libraries were prepared using the Nextera
562 technology (Illumina), and sequencing was performed on an MiSeq sequencer (2 × 75 bp)
563 through the Stanford Functional Genomics Facility. To analyze the genomic data, we used an
564 analysis pipeline adapted from GATK's recommended best practices (65–67). Reads were
565 mapped to *C. elegans* reference genome (WBcel 235.82) using the Bowtie 2 software (68).
566 Variant calling was performed using Haplotype Caller software from GATK, and lists from
567 AV913 and N2 were compared to eliminate non-causal variants. The predicted effects of
568 variants specific to AV913 were then annotated using SnpEff (69).

569 Initial genetic mapping experiments had placed *dsb-3(me6ts)* within 2 cM of *unc-5*,
570 located at 1.78 cM on chromosome IV; the above sequence analysis identified several
571 candidate mutations within this region. Additional mapping crosses located *dsb-3(me6ts)* to the
572 left of *dpy-20* (at 5.22 cM) and near or to the left of *unc-24* (at 3.51 cM). Further, we found that
573 *eDf18* (which deletes the region between 3.7- 4.19 cM) complements *dsb-3(me6ts)*. Together,
574 these experiments identified a G -> A transition at genomic position IV: 7758710 (WS279), in
575 the second coding exon of the uncharacterized gene *C46A5.5*, as the likely causal mutation
576 responsible for the *dsb-3(me6ts*) mutant phenotype.

577 <u>DAPI staining of oocyte chromosomes and Irradiation Assay</u>

578 Numbers of DNA bodies present in diakinesis oocytes were assessed in intact adult
579 hermaphrodites of the indicated ages, raised at the indicated temperatures, fixed in ethanol and
580 stained with 4′,6-diamidino-2-phenylindole (DAPI) as in (70). This method underestimates the
581 frequency of achiasmate chromosomes, as some univalents lie too close to each other to be
582 resolved unambiguously.

583 To test for rescue of bivalent formation by exogenously derived DSBs, worms were exposed to
584 5,000 rad (50 Gy) of γ-irradiation using a Cs-137 source at 20 h post-L4 stage. Worms were

585 fixed and stained at 18–20 h post-irradiation, and numbers of DAPI bodies were counted in
586 oocyte nuclei in the -1 to -3 positions.

587 Bioinformatic identification of homology between DSB-3 and Mei4

588 PSI Blast searches using the MPI BLAST server (71) , initiated using an alignment of DSB-3
589 homologs from diverse roundworm species as the query, identified a putative *Brugia malayi*
590 DSB-3 homolog. A subsequent round of PSI-BLAST searches, initiated using an alignment with
591 the putative *B. malayi* homolog as the header sequence and initially focusing on the N-terminal
592 portion of the protein, led to retrieval of plant and animal Mei4 homologs. Similarity in protein
593 lengths and patterns of predicted secondary structure were prioritized over E-value
594 considerations in selection of proteins chosen for the multiple sequence alignment presented in
595 Supplemental Figure 2, which was generated using MAFFT Version 7.0 with gap opening
596 penalty parameter set to 2.0 and offset value parament set to 0.125.

597 Yeast Two-Hybrid Analysis

598 Full-length DSB-1, DSB-2, DSB-3, and N-terminally truncated SPO-11 (SPO-11Δ1-47),
599 DSB-1 (DSB-1Δ1-33) ORFs were individually cloned into the *Bam*HI and *Pst*I sites of pBridge,
600 and the *Bam*HI and *Xho*I sites of pGADT7 (Clontech) to generate fusion proteins with the N-
601 terminal Gal4 DNA-binding domain (Gal4BD) or activation domain (Gal4AD). The PJ69-4A
602 yeast strain (*MATa trp1-901 leu2-3,112 ura3-52 his3-200 gal4Δ gal8Δ GAL2-ADE2*
603 *LYS2::GAL1-HIS3 met2::GAL7-lacZ*) was co-transformed with the indicated pairs of constructs
604 encoding Gal4BD and Gal4AD fusion proteins (and/or empty vector negative controls).
605 Transformed cells expressing Gal4BD and Gal4AD fusion proteins were selected in SD-Leu$^-$Trp$^-$
606 , a drop-out medium without leucine and tryptophan. Protein interactions were assayed by
607 growing transformed cells for 5 days at 30°C on selective media lacking leucine, tryptophan,
608 histidine, and adenine (SD-Leu$^-$Trp$^-$His$^-$Ade$^-$). Three independent repeats of each transformation

609 were performed for all pairwise combinations. The full-length SPO-11 ORF was excluded from
610 analysis of combinations as it exhibited autoactivation in negative control experiments.

611 Immunofluorescence Methods

612 The following primary antibodies were used: mouse anti-HA (1:1000, Covance 16B12
613 clone), rabbit anti-FLAG (1:5000, Sigma Aldrich), rabbit anti-DSB-2 (1:5.000, (20)), guinea pig
614 anti-DSB-1 (1:500, (21)), rabbit anti-GFP (1:200, (31)), guinea pig anti-HIM-8 (1:500, (32)),
615 chicken anti-HTP-3 (1:400, (33)), rabbit anti-SYP-2 (1:200, (35)), rat anti-RAD-51 (1:500, (20)),
616 guinea pig anti-SUN-1 S24pi (1:700, (72)), chicken anti-GFP (1:500, (A01694, Genscript)).
617 Secondary antibodies were Alexa Fluor 488, 555 and 647-conjugated goat antibodies directed
618 against the appropriate species (1:400, Life Technologies).

619 For immunofluorescence experiments involving whole mount gonads, dissection of
620 gonads, fixation, immuno-staining and DAPI counterstaining were performed as in (48) .

621 For experiments involving nuclear spreads, spreading was performed as in (73). The
622 gonads of 20–100 adult worms were dissected in 10 µL Dissection solution (75% v/v Hank's
623 Balanced Salt Solution [HBSS, Life Technology, 24020-117] with 0.1% v/v Tween-20) on an
624 ethanol-washed plain slide. 50 µL of spreading solution (32 µL of Fixative [4% w/v
625 Paraformaldehyde and 3.2%–3.6% w/v Sucrose in water], 16 µL of Lipsol solution [1% v/v in
626 water], 2 µL of Sarcosyl solution [1% w/v of Sarcosyl in water]) were added, and gonads were
627 immediately distributed over the whole slide using a pipette tip. Slides were then left to dry at
628 room temperature overnight, washed for 20 minutes in methanol at -20°C and rehydrated by
629 washing 3 times for 5 minutes in PBS-T. A 20-minute blocking in 1% w/v BSA in PBS-T at room
630 temperature was followed by overnight incubation with primary antibodies at room temperature
631 (antibodies diluted in: 1% w/v BSA in PBS-T). Slides were washed 3 times for 5 minutes in PBS-

632 T before secondary antibody incubation for 2 hours at room temperature. After PBS-T washes,
633 the samples were mounted in Vectashield (Vector).

634 To dissect large quantities of *C. elegans* gonads for spreads, we employed an
635 alternative method for disrupting worms, using a 125V ~ 60Hz drill capable of achieving 1,600
636 rotations per minute. Briefly, we synchronized worms by using the standard bleaching protocol
637 (74) and allowed worms grow to adulthood (L4 + 24 hours). The worms were then washed with
638 dissection solution into a 1.7 mL Eppendorf tube suspended in an ethanol ice bath. The worms
639 were then disrupted using a 1/64 inch bit on the drill with its maximum power by angling the drill
640 bit against the Eppendorf tube wall. 3 µL aliquots were taken from the tube every 20 seconds
641 and monitored microscopically until most of the gonads had been extruded from the worms
642 during the drill-induced disruption.

643 <u>FISH experiments</u>

644 Barcoded Oligopaint probes targeting a 1 Mb segment of chromosome II (genomic
645 coordinates 11,500,001-12,500,001) were generated as in (46). Gonads from animals at 24
646 hours after L4 were dissected on a coverslip and fixed in 1% paraformaldehyde for 5 min. A
647 slide (Superfrost Plus) was then placed on the coverslip and immersed in liquid N_2. The sample
648 was then incubated in −20°C methanol for 2 minutes and rehydrated by placing in PBST for at
649 least 10 minutes. Next, the sample was incubated in 0.1 M HCl for 5 minutes and washed in
650 PBST 3 times for 5 minutes each. The samples were then incubated for 5 minutes each in 2x
651 SSCT (2x saline sodium citrate with 0.1% Tween) solutions with increasing concentrations of
652 formamide: 0%, 5%, 10%, 25%, and 50%. The sample was then incubated in a prewarmed
653 42°C solution of 50% formamide in 2x SSCT for 1 hour. 2 µL of Oligopaint probe (1,000 ng/µL in
654 dH2O) was diluted into 30 µL of hybridization solution (50% formamide, 10% Dextran Sulfate,
655 2x SSC, 0.1% Tween-20) for each slide. After 1 hour incubation, slides were taken out of the
656 50% formamide solution, wiped, and incubated in 95% ethanol for 5 minutes. Then, the probe

657 hybridization solution was applied to the sample with a coverslip, and the sample was denatured
658 for 10 minutes at 77°C on a heat block. After denaturing, the sample was incubated with the
659 probe hybridization solution at 42°C overnight. The next day, samples were washed 2 times in
660 42°C 50% formamide in 2x SSCT for 30 minutes each, and the coverslip was removed from the
661 slide. Then, the sample was incubated for 5 minutes each in solutions with decreasing
662 concentrations of formamide in 2x SSCT: 25%, 10%, and 5%. Samples were then washed 2
663 times for 10 minutes each in 2x SSCT. The Oligopaint probes were visualized by hybridizing
664 Cy3-labelled oligos (agctgatcgtggcgttgatg) to the Oligopaint probe barcode sequence. To do
665 this, the Cy3-labelled probes (diluted 1:1000 in 25% ethylene carbonate in 2x SSC) were
666 applied to the sample with a coverslip and incubated for 15 minutes. Then, the sample was
667 washed and the coverslip was removed by incubating in 30% formamide solution in 2x SSCT for
668 3 min. The samples were then washed twice in 2x SSC and mounted in Vectashield.
669 For quantification of pairing between FISH signals, gonads were divided into 6 zones.
670 Zone 1 corresponds to the distal tip region of the gonad with only premeiotic nuclei. The gonad
671 region extending from the transition zone to the end of the pachytene stage was split up into 5
672 equally sized regions, Zones 2-6. The stitched image of the gonad was cropped into zones,
673 peaks of FISH signals were identified using ImageJ plugin 3D Maxima Finder (75). Each
674 identified peak was manually assigned to a nucleus, and distances between homologous signal
675 peaks in the same nucleus were calculated.

676 Image Acquisition

677 For spread nuclei, imaging, deconvolution, stitching and 3D-SIM reconstruction were
678 performed as in (73). Spreading results in squashing of *C. elegans* germline nuclei from 5 to 1-2
679 µm in thickness. 3D-SIM images were obtained as 125 nm spaced Z-stacks, using a 100x NA
680 1.40 objective on a DeltaVison OMX Blaze microscopy system, 3D-reconstructed and corrected

681 for registration using SoftWoRx. For display, images were projected using maximum intensity
682 projection in ImageJ or SoftWoRx.

683 For imaging of whole-mount gonads. wide field (WF) images were obtained as 200 nm
684 spaced Z-stacks, using a 100x NA 1.40 objective on a DeltaVison OMX Blaze microscopy
685 system, deconvolved and corrected for registration using SoftWoRx. Subsequently, gonads
686 were assembled using the "Grid/Collection" plugin (76) in ImageJ. For display, assembled
687 gonads were projected using maximum intensity projection in ImageJ.

688 For display, contrast and brightness were adjusted in individual color channels using
689 ImageJ.

690 Quantification of RAD-51 Foci and COSA-1 Foci

691 For quantification of RAD-51 foci in whole-mount gonads, at least three gonads were
692 counted per genotype. Gonads were divided into seven zones: the premeiotic zone (PM), which
693 includes all nuclei prior to the transition zone (where nuclei enter meiotic prophase), and six
694 consecutive equal-sized zones encompassing the region of the gonad from the transition zone
695 to the end of the pachytene stage. For the GFP::COSA-1 experiments, foci were counted in
696 nuclei within the last six cell rows of the gonad.

697 Identification of DSB Protein Foci and Object-Based Colocalization Analysis

698 For Figures 5 and 6, images were analyzed using an object-based colocalization
699 analysis pipeline that combined standard functions available in ImageJ in conjunction with a
700 custom Python script. A detailed description of the colocalization analysis pipeline is presented
701 in Supplemental Figure 3. For these analyses, 32-bit Z-stacks of SIM images of
702 immunofluorescence signals for at least two different antibodies detecting DSB proteins (C1 and
703 C2). were imported into ImageJ (77, 78) with the Fiji distribution (79). The signal maxima for

704 each channel, identified as foci by the image analysis pipeline were qualitatively compared to
705 the original image to verify accurate identification of foci.

706 For colocalization analysis of DSB-2 and DSB-3::GFP foci on super-spread nuclei
707 (Supplemental Figure S5), the same pipeline was used, except that foci were analyzed within
708 3.43 x 3.43 μm square ROIs located entirely within the spread (1-3 ROIs per nucleus).

709

710 Data and reagent availability

711 The original 32-bit individual nucleus ImageJ files, the segmented axis channel files, the
712 identified peaks, the values used for and the output position files from the 3D Maxima Finder for
713 each nucleus, the custom python script used to identify colocalization, and the resulting
714 spreadsheet files showing colocalization data for each nucleus will be made available from the
715 BioStudies Database, Accession Number S-BSST568.

716 Strains and primary images used in this research are available on request from A.M.V.
717 (annev@stanford.edu).

718

719 **Figures**

720 **Figure 1. Identification of *dsb-3* as a gene required for the formation of meiotic**
721 **crossovers.** (A) Representative images of DAPI-stained diakinesis-stage oocyte nuclei from
722 adult worms of the indicated genotypes fixed at 1 day post L4. Left: WT nucleus with six DAPI
723 bodies corresponding to six pairs of homologs connected by chiasmata (bivalents). Middle: *dsb-*
724 *3(me6ts)* nucleus with 9 DAPI bodies (3 bivalents and 6 univalents). Right: *dsb-3(me115)*
725 nucleus with 12 DAPI bodies (all univalents). Below: Graphs show quantification of the mean
726 number of DAPI bodies/ nucleus; error bars indicate standard deviation, and numbers in

727 parentheses indicate the numbers of nuclei assayed. Assays for WT and for *dsb-3(me115)*
728 homozygotes were performed at 20°C; assays for *dsb-3(me6ts)* homozygotes and *dsb-*
729 *3(me6ts)/dsb-3(me115)* heterozygotes were performed at 25°C. (B) Schematic showing the
730 *dsb-3* gene structure, with the positions and nature of mutations used in this work; white boxes
731 represent UTR sequences, black boxes represent exons, lines indicate introns. Scale bar
732 indicates 100 bp. (C) Top: Whole-mount immunofluorescence images of GFP::COSA-1 foci,
733 which correspond to the single CO site on each homolog pair, in nuclei at the late pachytene
734 stage. WT nuclei have 6 GFP::COSA-1 foci, while foci are reduced or absent entirely in the *dsb-*
735 *3(me115)* mutant. Below: Stacked bar graphs showing the distribution of GFP::COSA-1 foci
736 counts in nuclei from WT and *dsb-3(me115)* mutants. Mean numbers of GFP::COSA-1 foci per
737 nucleus are indicated, with the numbers of nuclei assayed in parentheses. (D) Homolog pairing
738 assayed by immunofluorescence of X-Chromosome pairing center binding protein HIM-8 (Top)
739 or fluorescence *in situ* hybridization FISH detecting a 1Mbp segment of chromosome II (Bottom)
740 in pachytene nuclei of whole-mount gonads. A single focus is observed in each nucleus,
741 indicating successful pairing between the homologs. Scale bar is 3.2 μm. (E)
742 Immunofluorescence image of SC components in late pachytene nuclei in a whole-mount gonad
743 from the *dsb-3(me115)* mutant. Axis protein HTP-3 and SC central region protein SYP-2
744 colocalize in continuous stretches between chromosome pairs, indicating successful synapsis.
745 Scale bar is 3.2 μm.

746

747 **Figure 2. DSB-3 is required for meiotic double-strand break formation.** (A) Left:
748 Immunofluorescence images of RAD-51 foci in early pachytene nuclei in whole-mount gonads.
749 RAD-51 foci mark sites of processed DSBs and are strongly reduced in the *dsb-3(me115)*
750 mutant. Right: Quantification of RAD-51 foci in whole-mount gonads (at least three gonads were
751 scored per genotype). Gonads were divided into seven zones: the premeiotic zone (PM), which

752 includes all nuclei prior to the transition zone (where nuclei enter meiotic prophase), and six
753 consecutive equal-sized zones encompassing the region of the gonad from the transition zone
754 to the end of the pachytene stage. (B) Rescue of chiasma formation in *dsb-3* mutants by γ-
755 irradiation induced DNA breaks. Graph showing the average numbers of DAPI bodies present
756 in diakinesis-stage oocytes of worms exposed to 5 kRad of γ-irradiation at 20 hours post L4,
757 and un-irradiated age-matched controls, fixed and stained with DAPI 18-20 hours post
758 irradiation.

759 **Figure 3. DSB-3 is concentrated in DSB-competent nuclei and is interdependent with**
760 **DSB-1 and DSB-2.** (A) Immunofluorescence image of a whole-mount hermaphrodite gonad
761 (from distal tip to end of pachytene) stained with DAPI and antibodies detecting DSB-3::GFP,
762 DSB-1, and DSB-2. Meiotic progression proceeds from left to right, as in the rest of the images
763 for this figure. DSB-3::GFP becomes concentrated in germ cell nuclei within the transition zone
764 (rectangular inset - top, soon after entry into meiotic prophase. The DSB-3 immunofluorescence
765 signal is strongest in early pachytene nuclei, then declines sharply in mid-pachytene, albeit with
766 a few outlier nuclei (square inset) in the late pachytene region of the gonad retaining a strong
767 DSB-3 signal. This pattern of appearance and disappearance of DSB-3 from germ cell nuclei is
768 similar to the patterns observed for the double-strand break promoting proteins DSB-1 and
769 DSB-2. (B) Immunofluorescence images of a whole-mount hermaphrodite gonads stained with
770 DAPI and antibody detecting DSB-3::GFP. DSB-3::GFP signal is not detected in the *dsb-1(null)*
771 mutant, and is strongly reduced and limited to a smaller region of the gonad in the *dsb-2(null)*
772 mutant. (C) Immunofluorescence images of gonads stained for DSB-1 (left) or DSB-2(right),
773 showing that DSB-1 and DSB-2 immunofluorescence signals are not detected in the *dsb-*
774 *3(me115)* mutant. Scale bars = 16.2 μm.

775 **Figure 4. Evidence that DSB-1, DSB-2 and DSB-3 form a complex homologous to the**
776 **yeast and mammalian REC114-MEI4 complexes.** (A) Left: Schematic diagram depicting the

777 positions of six short signature motifs (SSMs, blue boxes) previously defined for Mei4 homologs
778 in diverse species, indicating the three SSMs (1, 4 and 6) that are most strongly supported in *C.*
779 *elegans* DSB-3; gray boxes indicate positions that potentially correspond to SSMs 2, 3 and 5
780 based on a multiple sequence alignment (MSA) with vertebrate and marine invertebrate
781 homologs of similar size, but are less well conserved. Right: Aligned sequences of SSMs 1, 4
782 and 6 from *Mus musculus, Homo sapiens, Xenopus tropicalis, Danio rerio*, *Strongylocentrotus*
783 *purpuratus, Amphimedon queenslandica, Aplysia californica* and the following nematodes of the
784 genus *Caenorhabditis*: *C. nigoni, C. briggsae, C. sinica, C. remanei, C. latens, C. tropicalis, C.*
785 *elegans*. SSMs are cropped from an MSA generated in JalView (80) using the ClustalX coloring
786 scheme. For additional information, see Supplemental Figure 2 and Materials and Methods. (B)
787 Yeast two-hybrid assay revealing protein-protein interactions among the DSB-1, -2, and -3
788 proteins and between DSB-1 and SPO-11. Potential interactions between proteins fused with
789 the GAL4 activation domain (AD) and proteins fused with the GAL4 DNA binding domain (BD)
790 were assayed by growth on media lacking histidine and adenine. A construct producing an N-
791 terminal truncation of SPO-11 lacking the first 47 amino acids (Δ1-47) was used for these
792 analyses, as severe auto-activation was observed for full-length SPO-11. Negative controls
793 showing lack of auto-activation for the constructs used are presented in Supplemental Figure 2.
794 In addition to experiments using constructs expressing full-length DSB-1, some experiments
795 used a construct expressing an N-terminally truncated DSB-1 lacking the first 33 amino acids
796 (Δ1-33). A schematic summarizing the identified interactions is shown on the bottom right.

797

798 **Figure 5. DSB-3, DSB-2, and DSB-1 colocalize in meiotic nuclei.** (A) Schematic
799 summarizing the object-based image analysis pipeline used to assess colocalization of foci in
800 SIM immunofluorescence images of partially spread nuclei (see Materials and Methods and
801 Supplemental Figure 3 for more details). (B) Representative SIM immunofluorescence images

802 of individual spread nuclei stained with antibodies targeting the indicated DSB proteins; each
803 panel depicts a single Z slice from a 3D image stack. The following experiments are
804 represented in order from left to right: mouse monoclonal HA and rabbit polyclonal DSB-2
805 antibodies, both detecting the same 3xHA::DSB-2 tagged protein in a *3xha::dsb-2* II strain;
806 chicken GFP and rabbit DSB-2 antibodies, detecting DSB-3::GFP and DSB-2 in a *meSi7[dsb-*
807 *3::gfp]* II; *dsb-3(me115)* IV strain ; mouse HA and rabbit FLAG antibodies, detecting
808 3xHA::DSB-1 and 3xFLAG::DSB-3 in a *3xflag::dsb-3 3xha::dsb-1* IV strain; and mouse HA and
809 rabbit DSB-2 antibodies, detecting 3xHA::DSB-1 and DSB-2 in a *3xflag::dsb-3 3xha::dsb-1* IV
810 strain. Scale bar is 2 μm. (C) Quantification of DSB protein foci for the indicated pairwise
811 combinations; each data point represents the numbers of foci for the two analyzed channels in a
812 single nucleus. Spearman R values reported indicate that numbers of the two types of foci are
813 strongly correlated within nuclei. (D) Graphs showing the fraction of foci of a given type
814 (indicated by a single colored circle in the denominator in each schematic below the horizontal
815 axis) that are colocalized with the other type of focus analyzed in that same experiment
816 (colocalizing foci are represented by two colored circles in the numerator). For each pair of
817 focus types analyzed, two sets of experimental analyses (represented by colored data points)
818 and paired negative controls (represented by grey data points) are presented.

819

820 **Figure 6. The Presence and Colocalization of DSB-3, DSB-2, and DSB-1 are Not Confined**
821 **to the Meiotic Chromosomal Axis.** (A) Left: representative maximum-intensity projections of
822 SIM images, representing the middle third of Z-stacks collected for the depicted spread nuclei.
823 Nuclei were stained with antibodies targeting DSB proteins and the axis component HTP-3.
824 Scale bar is 2 μm. Right: graph showing quantification of numbers of DSB protein foci that
825 colocalize with the axis signal, as well as the total numbers of DSB protein foci identified in the
826 analyzed nuclei. The data indicate that the majority of foci do not colocalize with the axis. (B)

827 Graphs depicting the fractions of Colocalized Foci / Total Foci for DSB protein foci of the
828 indicated types (represented as in Figure 5), reported for axis-associated foci and for total
829 nuclear foci analyzed within the same data sets. The filled dots represent colocalization
830 fractions for all DSB protein foci of a given type within the nucleus, while dots with crosses
831 represent the colocalization fractions for the subset of DSB protein foci of the indicated type that
832 colocalize with the axis.

833

834 **Table 1. Quantitation of embryo viability, male frequency and diakinesis karyotypes.**
835 Strains used in and/or created for this study were evaluated for the indicated parameters.
836 Numbers of DAPI bodies were evaluated for worms fixed and stained at 24 hours post L4 stage.
837 Analysis of AV913 and corresponding controls were conducted at two temperatures based on
838 the temperature-sensitive nature of the *dsb-3(me6ts)* mutant.

839 **Supplemental Table 1. Summary of information relevant to the CRISPR/Cas9 edits**
840 **created for this work**. Information includes: a) sequence of the cRNA used in the injection
841 mixture; b) sequence of the edit created and description of its effect on the gene and encoded
842 protein; c) sequences of primers used for mutation detection and verification of edits via Sanger
843 sequencing.

844 **Supplemental Figure 1. Meiotic prophase progression and homolog pairing in the *dsb-***
845 ***3(null)* mutant.** (A) Immunofluorescence images of whole-mount hermaphrodite gonads (from
846 distal tip to end of pachytene) stained with DAPI and antibodies detecting SUN-1 Ser24 Pi, an
847 indicator of CHK-2 activity detected from the onset of meiotic prophase through the early
848 pachytene stage (36, 72). *dsb-3(me115)* mutant germlines shown an extension of this marker
849 relative to WT, reflecting operation of a crossover assurance checkpoint/surveillance
850 mechanism that prolongs the early pachytene stage in response to one or more chromosome

851 pairs lacking crossover-competent recombination intermediates (20, 21, 36). (B) Quantification
852 of homolog pairing assayed by FISH. FISH signals from homologous chromosomes were
853 considered paired if they were separated by ≤ 0.7 μm. Numbers of nuclei scored for WT: zone
854 1, n=180; zone 2, n=201; zone 3, n=180; zone 4, n=178; zone 5, n=180; zone 6, n=167.
855 Numbers of nuclei scored for *dsb-3*: zone 1, n=159; zone 2, n=180; zone 3, n=155; zone 4,
856 n=160; zone 5, n=143; zone 6, n=117

857

858 **Supplemental Figure 2. Alignment of MEI4 and DSB-3 orthologs, and Y2H controls.** (A)
859 Multiple sequence alignment generated with MAFFT Version 7.0 with the ClustalX coloring
860 scheme. Protein sequences included in the multiple sequence alignment were from the
861 following species: Vertebrates: *Mus musculus, Homo sapiens, Xenopus tropicalis, Danio rerio*;
862 marine invertebrates: *Strongylocentrotus purpuratus, Amphimedon queenslandica, Aplysia*
863 *californica*; Nematodes of the genus *Caenorhabditis*: *C. nigoni, C. briggsae, C. sinica, C.*
864 *remanei, C. latens, C. tropicalis, C. elegans*. The outlined boxes indicate the positions of the
865 SSMs that were previously defined for MEI4 orthologs from diverse species. Red boxes indicate
866 cases where the SSM includes at least 5 amino acid residues that are conserved or exhibit
867 similar electrophysiological properties in at least 85% of the aligned sequences. Gray boxes
868 indicate cases where these thresholds are not met. (B) Negative controls for yeast two-hybrid
869 assays, showing lack of auto-activation for cells containing the indicated constructs.

870 **Supplemental Figure 3. 3D Object-Based Colocalization Analysis Pipeline for SIM images**
871 **of DSB protein foci in spread nuclei.** (A) A schematic showing the general pipeline used for
872 colocalization analyses. ImageJ plugins used were 3D Maxima Finder (75) and the 3D Object
873 Counter (81). (B) Yellow box indicating protocol used in a subset of our analyses in which
874 images were additionally segmented to identify DSB protein foci that coincided with the axis
875 signal; the Otsu method (82) was used in our thresholding process for this segmentation.

876 **Supplemental Figure 4. Cumulative distribution plots for the distances from each**
877 **Channel 1 DSB protein focus to its nearest neighbor Channel 2 focus.** The x-axis
878 represents the distances between nearest neighbor foci pairs, and the y-axis indicates the
879 percentage of measurements at or below the given distance on the x-axis. Experimental data
880 are depicted in green circles and values for the corresponding negative control rotated images
881 are indicated with purple squares. (A) The cumulative distribution of distances between
882 3xHA::DSB-2 mAB foci and nearest neighbor DSB-2 pAB foci. (B) The cumulative distribution
883 of distances between 3xHA::DSB-1 foci and nearest neighbor 3xFLAG::DSB-3 foci. (C) The
884 cumulative distribution of distances between 3xHA::DSB-1 foci and nearest neighbor DSB-2
885 pAB foci. (D) The cumulative distribution of distances between DSB-3::GFP foci and nearest
886 neighbor DSB-2 pAB foci.

887 **Supplemental Figure 5. Colocalization analysis for DSB-2 and DSB-3::GFP on super-**
888 **spread nuclei.** Images depict a super-spread nucleus (top) and an inset from the same
889 nucleus (bottom), showing DAPI-stained DNA and immunofluorescence signals corresponding
890 to DSB-2, DSB-3::GFP, and axis protein HTP-3. The graph shows the fraction of DSB-2 foci
891 (magenta) within a given ROI that are colocalized with a DSB-3::GFP focus (green), and vice
892 versa, together with their paired negative controls (represented by grey data points).

893

894 **Acknowledgments**

895 We are grateful to C. Girard and S. Ramakrishnan for assistance with irradiation experiments
896 and generation of sequencing libraries, W. Zhang for crosses performed early in the analysis of
897 the *me6ts* mutant, and David Paul for discussions regarding object-based colocalization
898 analysis. We acknowledge N. Bhatla for creating the Exon-Intron Graphic Maker (wormweb.org)
899 used for Figure 1B. We thank A. Dernburg and V. Jantsch for antibodies and the Caenorhabditis

Genetics Center (funded by NIH Office of Research Infrastructure Programs P40 OD010440) for strains. This work was supported by an American Cancer Society Research Professor Award (RP-15-209-01-DDC) and NIH grants R01GM53804 and R35GM126964 to AMV, by a Blavatnik Family Foundation Fellowship and a Stanford Mason Case Fellowship to AH, by an FWF Erwin Schrödinger Fellowship (J-3676) to AW, by a Stanford Graduate Fellowship to KY, by grants from the Taiwan Ministry of Science and Technology (107-2923-B-002-001-MY4 and MoST 104-2628-B-002-002-MY3) to PC, and by grant 1S10OD01227601 from the NCRR to the Stanford Cell Sciences Imaging Facility.

References

1. S. Keeney, “Spo11 and the Formation of DNA Double-Strand Breaks in Meiosis” in *Recombination and Meiosis*, Genome Dynamics and Stability., R. Egel, D.-H. Lankenau, Eds. (Springer Berlin Heidelberg, 2008), pp. 81–123.

2. S. Keeney, J. Lange, N. Mohibullah, Self-Organization of Meiotic Recombination Initiation: General Principles and Molecular Pathways. *Annu. Rev. Genet.* **48**, 187–214 (2014).

3. S. Keeney, C. N. Giroux, N. Kleckner, Meiosis-Specific DNA Double-Strand Breaks Are Catalyzed by Spo11, a Member of a Widely Conserved Protein Family. *Cell* **88**, 375–384 (1997).

4. A. Bergerat, *et al.*, An atypical topoisomerase II from archaea with implications for meiotic recombination. *Nature* **386**, 414–417 (1997).

5. K. S. McKim, Meiotic Synapsis in the Absence of Recombination. *Science* **279**, 876–878 (1998).

6. A. F. Dernburg, *et al.*, Meiotic Recombination in C. elegans Initiates by a Conserved Mechanism and Is Dispensable for Homologous Chromosome Synapsis. *Cell* **94**, 387–398 (1998).

7. T. Robert, *et al.*, The TopoVIB-Like protein family is required for meiotic DNA double-strand break formation. *Science* **351**, 943–949 (2016).

8. N. Vrielynck, *et al.*, A DNA topoisomerase VI-like complex initiates meiotic recombination. *Science* **351**, 939–943 (2016).

930 9. C. Claeys Bouuaert, *et al.*, Structural and functional characterization of the Spo11 core
931 complex. *Nat. Struct. Mol. Biol.* **28**, 92–102 (2021).

932 10. T. M. Menees, G. S. Roeder, MEI4, a yeast gene required for meiotic recombination.
933 *Genetics* **123**, 675–682 (1989).

934 11. R. E. Malone, D. L. Pittman, J. J. Nau, Examination of the Intron in the meiosis-specific
935 recombination gene REC114 in Saccharomyces. *Mol. Gen. Genet. MGG* **255**, 410–419
936 (1997).

937 12. S. Tessé, *et al.*, Asy2/Mer2: an evolutionarily conserved mediator of meiotic recombination,
938 pairing, and global chromosome compaction. *Genes Dev.* **31**, 1880–1893 (2017).

939 13. R. Kumar, H.-M. Bourbon, B. de Massy, Functional conservation of Mei4 for meiotic DNA
940 double-strand break formation from yeasts to mice. *Genes Dev.* **24**, 1266–1280 (2010).

941 14. R. Kumar, *et al.*, MEI4 – a central player in the regulation of meiotic DNA double-strand
942 break formation in the mouse. *J. Cell Sci.* **128**, 1800–1811 (2015).

943 15. R. Kumar, *et al.*, Mouse REC114 is essential for meiotic DNA double-strand break
944 formation and forms a complex with MEI4. *Life Sci. Alliance* **1**, e201800259 (2018).

945 16. M. Molnar, *et al.*, Characterization of rec7, an early meiotic recombination gene in
946 Schizosaccharomyces pombe. *Genetics* **157**, 519–532 (2001).

947 17. S. Bonfils, A. E. Rozalen, G. R. Smith, S. Moreno, C. Martin-Castellanos, Functional
948 interactions of Rec24, the fission yeast ortholog of mouse Mei4, with the meiotic
949 recombination-initiation complex. *J. Cell Sci.* **124**, 1328–1338 (2011).

950 18. A. De Muyt, *et al.*, A high throughput genetic screen identifies new early meiotic
951 recombination functions in Arabidopsis thaliana. *PLoS Genet.* **5**, e1000654 (2009).

952 19. A. Ronceret, M.-P. Doutriaux, I. N. Golubovskaya, W. P. Pawlowski, PHS1 regulates
953 meiotic recombination and homologous chromosome pairing by controlling the transport of
954 RAD50 to the nucleus. *Proc. Natl. Acad. Sci. U. S. A.* **106**, 20121–20126 (2009).

955 20. S. Rosu, *et al.*, The C. elegans DSB-2 Protein Reveals a Regulatory Network that Controls
956 Competence for Meiotic DSB Formation and Promotes Crossover Assurance. *PLoS*
957 *Genet.* **9**, e1003674 (2013).

958 21. E. L. Stamper, *et al.*, Identification of DSB-1, a Protein Required for Initiation of Meiotic
959 Recombination in Caenorhabditis elegans, Illuminates a Crossover Assurance Checkpoint.
960 *PLoS Genet.* **9**, e1003679 (2013).

961 22. J. Li, G. W. Hooker, G. S. Roeder, Saccharomyces cerevisiae Mer2, Mei4 and Rec114
962 Form a Complex Required for Meiotic Double-Strand Break Formation. *Genetics* **173**,
963 1969–1981 (2006).

964 23. S. Maleki, M. J. Neale, C. Arora, K. A. Henderson, S. Keeney, Interactions between Mei4,
965 Rec114, and other proteins required for meiotic DNA double-strand break formation in
966 Saccharomyces cerevisiae. *Chromosoma* **116**, 471–486 (2007).

967 24. S. Steiner, J. Kohli, K. Ludin, Functional interactions among members of the meiotic
968 initiation complex in fission yeast. *Curr. Genet.* **56**, 237–249 (2010).

969 25. T. Miyoshi, *et al.*, A Central Coupler for Recombination Initiation Linking Chromosome
970 Architecture to S Phase Checkpoint. *Mol. Cell* **47**, 722–733 (2012).

971 26. M. Stanzione, *et al.*, Meiotic DNA break formation requires the unsynapsed chromosome
972 axis-binding protein IHO1 (CCDC36) in mice. *Nat. Cell Biol.* **18**, 1208–1220 (2016).

973 27. C. Claeys Bouuaert, *et al.*, DNA-driven condensation assembles the meiotic DNA break
974 machinery. *Nature* **592**, 144–149 (2021).

975 28. S. Panizza, *et al.*, Spo11-Accessory Proteins Link Double-Strand Break Sites to the
976 Chromosome Axis in Early Meiotic Recombination. *Cell* **146**, 372–383 (2011).

977 29. H. Sasanuma, *et al.*, Cdc7-dependent phosphorylation of Mer2 facilitates initiation of yeast
978 meiotic recombination. *Genes Dev.* **22**, 398–410 (2008).

979 30. J. A. Carballo, *et al.*, Budding Yeast ATM/ATR Control Meiotic Double-Strand Break (DSB)
980 Levels by Down-Regulating Rec114, an Essential Component of the DSB-machinery.
981 *PLoS Genet.* **9**, e1003545 (2013).

982 31. R. Yokoo, *et al.*, COSA-1 Reveals Robust Homeostasis and Separable Licensing and
983 Reinforcement Steps Governing Meiotic Crossovers. *Cell* **149**, 75–87 (2012).

984 32. C. M. Phillips, *et al.*, HIM-8 Binds to the X Chromosome Pairing Center and Mediates
985 Chromosome-Specific Meiotic Synapsis. *Cell* **123**, 1051–1063 (2005).

986 33. A. J. MacQueen, *et al.*, Chromosome Sites Play Dual Roles to Establish Homologous
987 Synapsis during Meiosis in C. elegans. *Cell* **123**, 1037–1050 (2005).

988 34. A. F. Severson, L. Ling, V. van Zuylen, B. J. Meyer, The axial element protein HTP-3
989 promotes cohesin loading and meiotic axis assembly in C. elegans to implement the
990 meiotic program of chromosome segregation. *Genes Dev.* **23**, 1763–1778 (2009).

991 35. M. P. Colaiácovo, *et al.*, Synaptonemal Complex Assembly in C. elegans Is Dispensable
992 for Loading Strand-Exchange Proteins but Critical for Proper Completion of
993 Recombination. *Dev. Cell* **5**, 463–474 (2003).

994 36. A. Woglar, *et al.*, Matefin/SUN-1 Phosphorylation Is Part of a Surveillance Mechanism to
995 Coordinate Chromosome Synapsis and Recombination with Meiotic Progression and
996 Chromosome Movement. *PLoS Genet.* **9**, e1003335 (2013).

997 37. F. Pâques, J. E. Haber, Multiple pathways of recombination induced by double-strand
998 breaks in Saccharomyces cerevisiae. *Microbiol. Mol. Biol. Rev. MMBR* **63**, 349–404
999 (1999).

1000 38. P. Sung, Catalysis of ATP-dependent homologous DNA pairing and strand exchange by
1001 yeast RAD51 protein. *Science* **265**, 1241–1243 (1994).

1002 39. A. Alpi, P. Pasierbek, A. Gartner, J. Loidl, Genetic and cytological characterization of the
1003 recombination protein RAD-51 in Caenorhabditis elegans. *Chromosoma* **112**, 6–16 (2003).

1004 40. H.-M. Bourbon, Comparative genomics supports a deep evolutionary origin for the large,
1005 four-module transcriptional mediator complex. *Nucleic Acids Res.* **36**, 3993–4008 (2008).

1006 41. L. A. Kelley, S. Mezulis, C. M. Yates, M. N. Wass, M. J. E. Sternberg, The Phyre2 web
1007 portal for protein modeling, prediction and analysis. *Nat. Protoc.* **10**, 845–858 (2015).

1008 42. M. Boekhout, *et al.*, REC114 Partner ANKRD31 Controls Number, Timing, and Location of
1009 Meiotic DNA Breaks. *Mol. Cell* **74**, 1053-1068.e8 (2019).

1010 43. C. Arora, K. Kee, S. Maleki, S. Keeney, Antiviral Protein Ski8 Is a Direct Partner of Spo11
1011 in Meiotic DNA Break Formation, Independent of Its Cytoplasmic Role in RNA Metabolism.
1012 *Mol. Cell* **13**, 549–559 (2004).

1013 44. A. Woglar, A. M. Villeneuve, Dynamic Architecture of DNA Repair Complexes and the
1014 Synaptonemal Complex at Sites of Meiotic Recombination. *Cell* **173**, 1678-1691.e16
1015 (2018).

1016 45. M. G. L. Gustafsson, Nonlinear structured-illumination microscopy: Wide-field fluorescence
1017 imaging with theoretically unlimited resolution. *Proc. Natl. Acad. Sci.* **102**, 13081–13086
1018 (2005).

1019 46. A. Woglar, *et al.*, Quantitative cytogenetics reveals molecular stoichiometry and
1020 longitudinal organization of meiotic chromosome axes and loops. *PLOS Biol.* **18**, e3000817
1021 (2020).

1022 47. F. Couteau, HTP-1 coordinates synaptonemal complex assembly with homolog alignment
1023 during meiosis in C. elegans. *Genes Dev.* **19**, 2744–2756 (2005).

1024 48. E. Martinez-Perez, HTP-1-dependent constraints coordinate homolog pairing and synapsis
1025 and promote chiasma formation during C. elegans meiosis. *Genes Dev.* **19**, 2727–2743
1026 (2005).

1027 49. W. Goodyer, *et al.*, HTP-3 Links DSB Formation with Homolog Pairing and Crossing Over
1028 during C. elegans Meiosis. *Dev. Cell* **14**, 263–274 (2008).

1029 50. Y. Kim, *et al.*, The chromosome axis controls meiotic events through a hierarchical
1030 assembly of HORMA domain proteins. *Dev. Cell* **31**, 487–502 (2014).

1031 51. T. Kaur, M. V. Rockman, Crossover heterogeneity in the absence of hotspots in
1032 Caenorhabditis elegans. *Genetics* **196**, 137–148 (2014).

1033 52. M. R. Bernstein, M. V. Rockman, Fine-Scale Crossover Rate Variation on the
1034 Caenorhabditis elegans X Chromosome. *G3 Bethesda Md* **6**, 1767–1776 (2016).

1035 53. F. Baudat, K. Manova, J. P. Yuen, M. Jasin, S. Keeney, Chromosome synapsis defects
1036 and sexually dimorphic meiotic progression in mice lacking Spo11. *Mol. Cell* **6**, 989–998
1037 (2000).

1038 54. P. J. Romanienko, R. D. Camerini-Otero, The mouse Spo11 gene is required for meiotic
1039 chromosome synapsis. *Mol. Cell* **6**, 975–987 (2000).

1040 55. K. J. Hillers, V. Jantsch, E. Martinez-Perez, J. L. Yanowitz, Meiosis. *WormBook Online*
1041 *Rev. C Elegans Biol.* **2017**, 1–43 (2017).

1042 56. W. J. Swanson, V. D. Vacquier, The rapid evolution of reproductive proteins. *Nat. Rev.*
1043 *Genet.* **3**, 137–144 (2002).

1044 57. A. L. Dapper, B. A. Payseur, Molecular evolution of the meiotic recombination pathway in
1045 mammals. *Evol. Int. J. Org. Evol.* **73**, 2368–2389 (2019).

1046 58. S. Brenner, The genetics of Caenorhabditis elegans. *Genetics* **77**, 71–94 (1974).

1047 59. C. Frøkjaer-Jensen, *et al.*, Single-copy insertion of transgenes in Caenorhabditis elegans.
1048 *Nat. Genet.* **40**, 1375–1383 (2008).

1049 60. C. Frøkjær-Jensen, *et al.*, An Abundant Class of Non-coding DNA Can Prevent Stochastic
1050 Gene Silencing in the C. elegans Germline. *Cell* **166**, 343–357 (2016).

1051 61. C. Engler, R. Kandzia, S. Marillonnet, A One Pot, One Step, Precision Cloning Method with
1052 High Throughput Capability. *PLoS ONE* **3**, e3647 (2008).

1053 62. A. Paix, A. Folkmann, D. Rasoloson, G. Seydoux, High Efficiency, Homology-Directed
1054 Genome Editing in *Caenorhabditis elegans* Using CRISPR-Cas9 Ribonucleoprotein
1055 Complexes. *Genetics* **201**, 47–54 (2015).

1056 63. J. A. Arribere, *et al.*, Efficient Marker-Free Recovery of Custom Genetic Modifications with
1057 CRISPR/Cas9 in *Caenorhabditis elegans*. *Genetics* **198**, 837–846 (2014).

1058 64. A. M. Villeneuve, A cis-acting locus that promotes crossing over between X chromosomes
1059 in Caenorhabditis elegans. *Genetics* **136**, 887–902 (1994).

1060 65. G. A. Auwera, *et al.*, From FastQ Data to High-Confidence Variant Calls: The Genome
1061 Analysis Toolkit Best Practices Pipeline. *Curr. Protoc. Bioinforma.* **43** (2013).

1062 66. M. A. DePristo, *et al.*, A framework for variation discovery and genotyping using next-
1063 generation DNA sequencing data. *Nat. Genet.* **43**, 491–498 (2011).

1064 67. A. McKenna, *et al.*, The Genome Analysis Toolkit: A MapReduce framework for analyzing
1065 next-generation DNA sequencing data. *Genome Res.* **20**, 1297–1303 (2010).

1066 68. B. Langmead, S. L. Salzberg, Fast gapped-read alignment with Bowtie 2. *Nat. Methods* **9**,
1067 357–359 (2012).

1068 69. P. Cingolani, *et al.*, A program for annotating and predicting the effects of single nucleotide
1069 polymorphisms, SnpEff: SNPs in the genome of Drosophila melanogaster strain w1118;
1070 iso-2; iso-3. *Fly (Austin)* **6**, 80–92 (2012).

1071 70. J. B. Bessler, K. C. Reddy, M. Hayashi, J. Hodgkin, A. M. Villeneuve, A Role for
1072 *Caenorhabditis elegans* Chromatin-Associated Protein HIM-17 in the Proliferation *vs* .
1073 Meiotic Entry Decision. *Genetics* **175**, 2029–2037 (2007).

1074 71. F. Gabler, *et al.*, Protein Sequence Analysis Using the MPI Bioinformatics Toolkit. *Curr.*
1075 *Protoc. Bioinforma.* **72**, e108 (2020).

1076 72. A. M. Penkner, *et al.*, Meiotic Chromosome Homology Search Involves Modifications of the
1077 Nuclear Envelope Protein Matefin/SUN-1. *Cell* **139**, 920–933 (2009).

1078 73. D. Pattabiraman, B. Roelens, A. Woglar, A. M. Villeneuve, Meiotic recombination
1079 modulates the structure and dynamics of the synaptonemal complex during C. elegans
1080 meiosis. *PLOS Genet.* **13**, e1006670 (2017).

1081 74. T. Stiernagle, Maintenance of C. elegans. *WormBook* (2006)
1082 https:/doi.org/10.1895/wormbook.1.101.1 (December 20, 2020).

1083 75. J. Ollion, J. Cochennec, F. Loll, C. Escudé, T. Boudier, TANGO: a generic tool for high-
1084 throughput 3D image analysis for studying nuclear organization. *Bioinformatics* **29**, 1840–
1085 1841 (2013).

1086 76. S. Preibisch, S. Saalfeld, P. Tomancak, Globally optimal stitching of tiled 3D microscopic
1087 image acquisitions. *Bioinforma. Oxf. Engl.* **25**, 1463–1465 (2009).

1088 77. C. T. Rueden, *et al.*, ImageJ2: ImageJ for the next generation of scientific image data.
1089 *BMC Bioinformatics* **18**, 529 (2017).

1090 78. C. A. Schneider, W. S. Rasband, K. W. Eliceiri, NIH Image to ImageJ: 25 years of image
1091 analysis. *Nat. Methods* **9**, 671–675 (2012).

1092 79. J. Schindelin, *et al.*, Fiji: an open-source platform for biological-image analysis. *Nat.*
1093 *Methods* **9**, 676–682 (2012).

1094 80. A. M. Waterhouse, J. B. Procter, D. M. A. Martin, M. Clamp, G. J. Barton, Jalview Version
1095 2--a multiple sequence alignment editor and analysis workbench. *Bioinforma. Oxf. Engl.*
1096 **25**, 1189–1191 (2009).

1097 81. S. Bolte, F. P. Cordelières, A guided tour into subcellular colocalization analysis in light
1098 microscopy. *J. Microsc.* **224**, 213–232 (2006).

1099 82. N. Otsu, A Threshold Selection Method from Gray-Level Histograms. *IEEE Trans. Syst.*
1100 *Man Cybern.* **9**, 62–66 (1979).

1101

						Average DAPI Bodies/Nucleus ± SD (number of oocytes)	
Strain	Genotype	Incubated Temperature	Average Brood Size ± SD (number of broods)	Percent Dead Eggs	Percent Males	*24 h post L4*	*48 h post L4*
N2	WT	20°	264 ± 27 (7)	0.4	0	6.0 ± 0.2 (92)	5.9 ± 0.3 (102)
N2	WT	25°	291 ± 22 (7)	2	0	5.9 ± 0.3 (110)	5.9 ± 0.4 (99)
AV913	*dsb-3(me6ts)* IV	20°	274 ± 27 (7)	0.1	0	6.0 ± 0.2 (144)	5.9 ± 0.3 (111)
AV913	*dsb-3(me6ts)* IV	25°	198 ± 47 (7)	28.2	17.3	7.0 ± 1.4 (108)	9.9 ± 1.3 (99)
AV1095	*dsb-3(me115)* IV	20°	156 ± 77 (16)	99.4	24.9	11.6 ± 0.6 (150)	
AV1029	*meSi7[sun1p::dsb-3::gfp::sun1 3'UTR unc-119+]* II; *dsb-3(me115)* IV	20°	150 ± 23 (8)	5	3.7	6.1 ± 0.4 (207)	
AV1102	*dsb-3(me125)[3xflag::dsb-3] dsb-1(me124)[3xha::dsb-1] IV*	20°	243 ± 34 (7)	2.1	2.5	6.0 ± 0.2 (213)	
AV1115	*dsb-2(me132)[3xha::dsb-2]* II	20°	193 ± 61 (8)	2.2	0.5	6.0 ± 0.2 (150)	

***dsb-1(me124) [3xha::dsb-1]* IV**

crRNA	CACUGGAGUGUCUGCAAUUC
Edit	ATGtatccatacgatgtcccagattacgcttacccatatgacgttccagactatgcctatccatacgatgtcccagattacgctTTTCCTGA**G**TT**A**CA**A**AC**G**CT**T**CA**A**TG
Description	Insertion of 3 N-terminal HA tags underlined and silent mutations introduced to the guide in bold.
Primers	TGTGAATCATTGCTCCCAAG, CCGTCAGCTTCCTGCTATTC

***dsb-3(me125) [3xflag::dsb-3]* IV**

crRNA	GAUCGAAAUUACCGAUGAUG
Edit	ATGgattataaagacgatgacgataagcgtgactacaaggacgacgacgacaagcgtgattacaaggatgacgatgacaagATCGAAATTACCGATGATGA**A**G
Description	Insertion of 3 N-terminal FLAG tags underlined and a silent PAM mutation in bold.
Primers	TTTTCCCGAAACACGATTCT, TTCGGAGTTACGACATCTGC

***dsb-3(me115)* IV**

crRNA	GAUCGAAAUUACCGAUGAUG
Edit	ATGATCGAAATTACCGATGATGAGGACTG**A**TTCC*GGTCTC*TGACTGACTGAACTGC~~T~~GTGTCTTAGCGTTTT
Description	*Leu9X* in bold: Insertion of a BsaI restriction site in italics; STOP codons in +1, +2, +3 frame underlined; and a silent PAM mutation in strikethrough.
Primers	ACACACGCCATCAAGAAAAGCA, TGTGAAGGAAACCGAGTTCCC

***dsb-2(me132) [3xha::dsb-2]* IV**

crRNA	UGUAGUACAUCUCAACUUUC
Edit	ATGtatccatacgatgtcccagattacgcttacccatatgacgttccagactatgcctatccatacgatgtcccagattacgctAGTGCACGTGG**A**CT
Description	Insertion of 3 N-terminal HA tags underlined and silent PAM mutation in bold.
Primers	TGAAGGGACCTGCGCGATGTTT, ATTGCGGTGTCCAGCAGGCATC

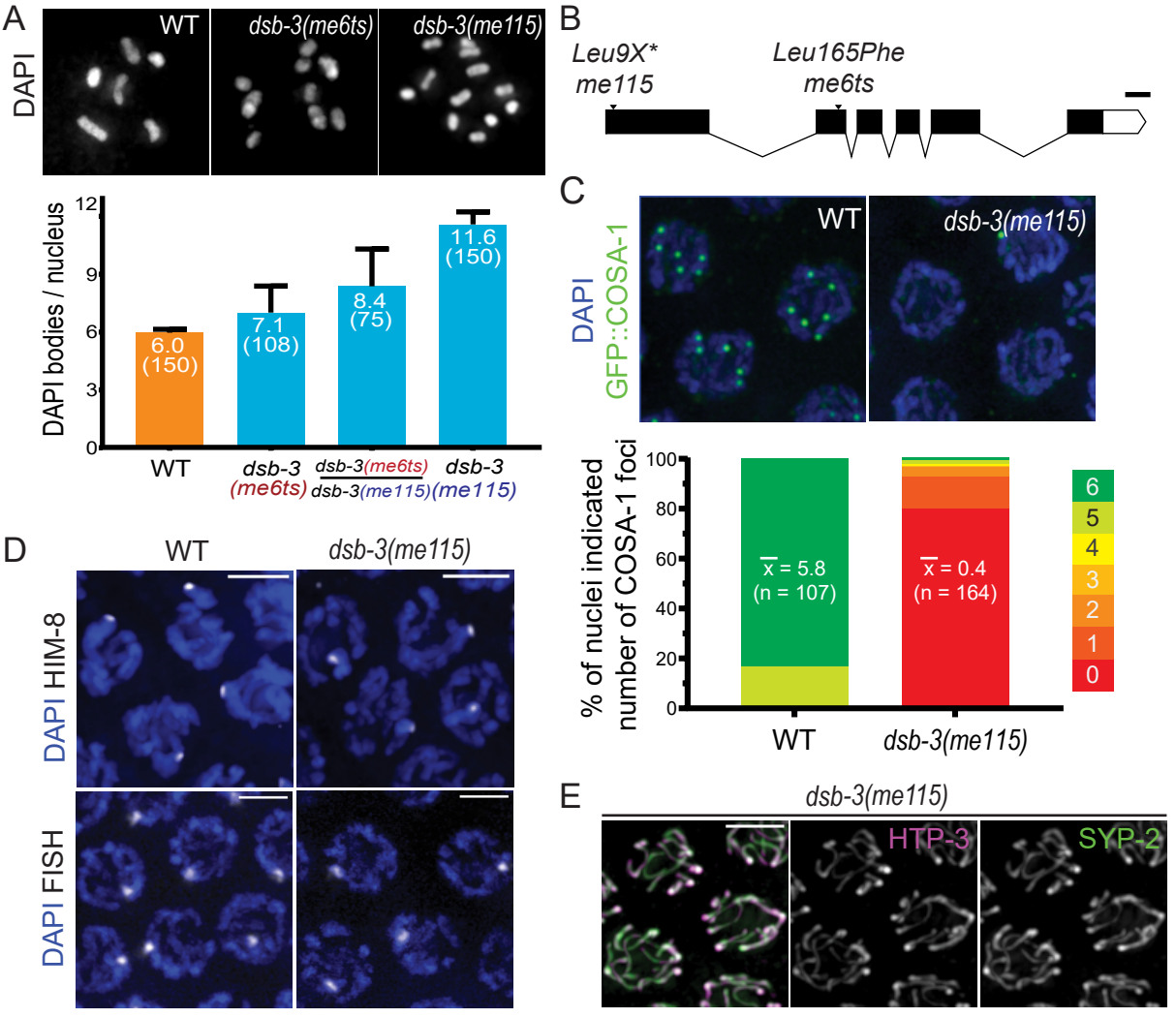
A
DAPI
WT
dsb-3(me6ts)
dsb-3(me115)
DAPI bodies / nucleus
12
9
6
3
0
6.0
(150)
7.1
(108)
8.4
(75)
11.6
(150)
WT
dsb-3
(me6ts)
dsb-3(me6ts)
dsb-3(me115)
dsb-3
(me115)
B
Leu9X*
me115
Leu165Phe
me6ts
C
DAPI
GFP::COSA-1
WT
dsb-3(me115)
% of nuclei indicated
number of COSA-1 foci
100
80
60
40
20
0
x̄ = 5.8
(n = 107)
x̄ = 0.4
(n = 164)
6
5
4
3
2
1
0
WT
dsb-3(me115)
D
WT
dsb-3(me115)
DAPI HIM-8
DAPI FISH
E
dsb-3(me115)
HTP-3
SYP-2

A

WT

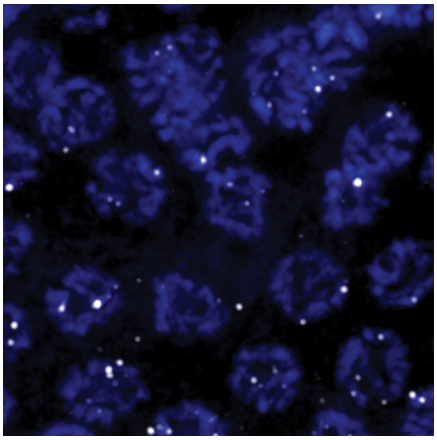

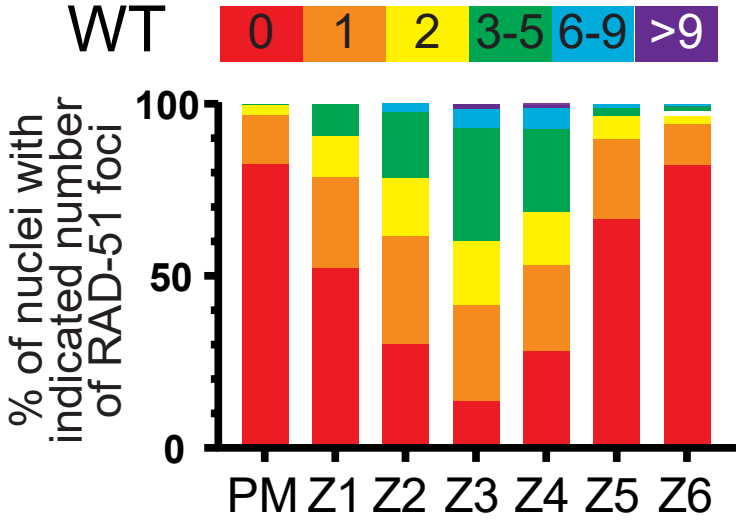

dsb-3(me115)

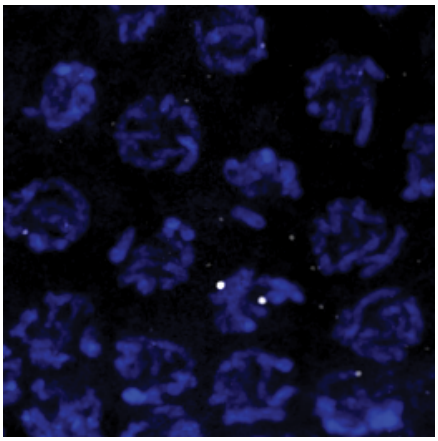

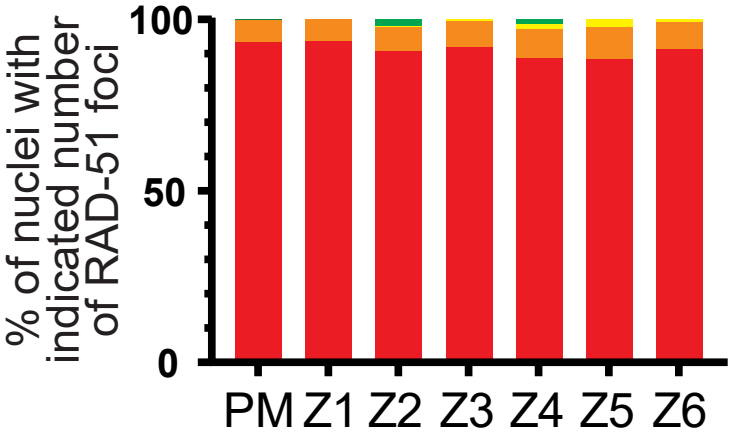

B

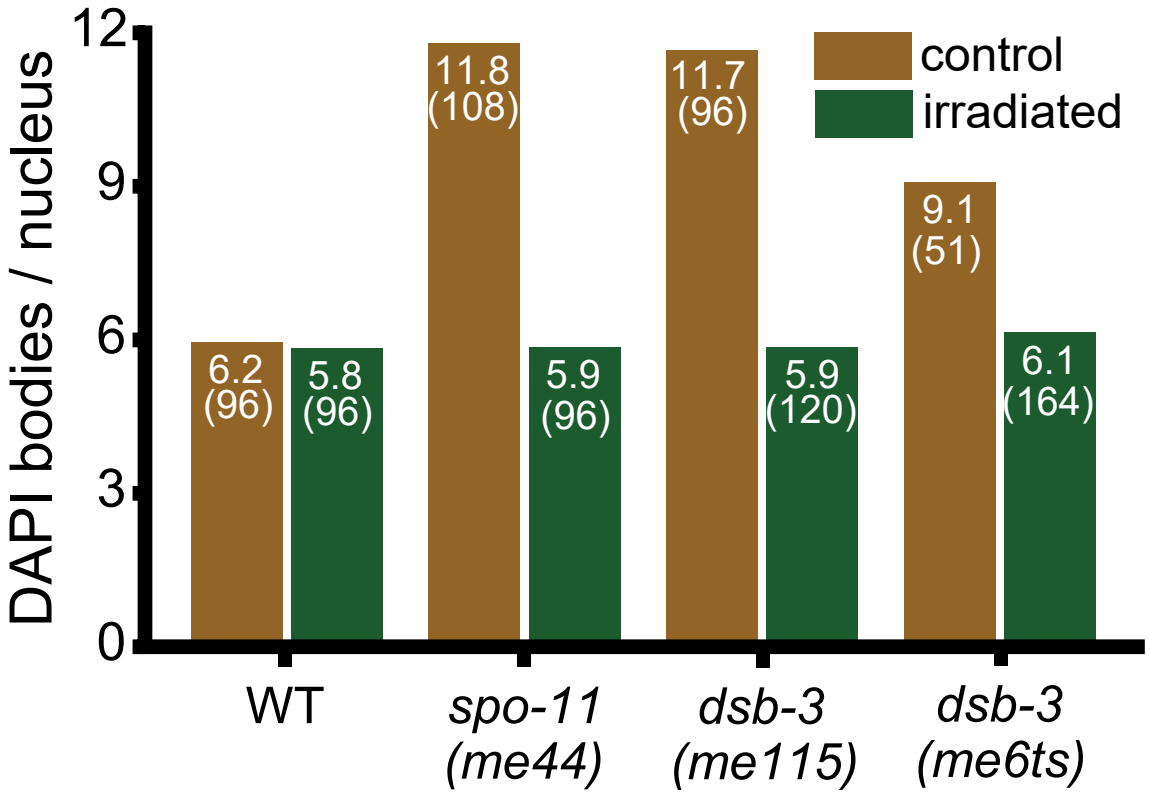

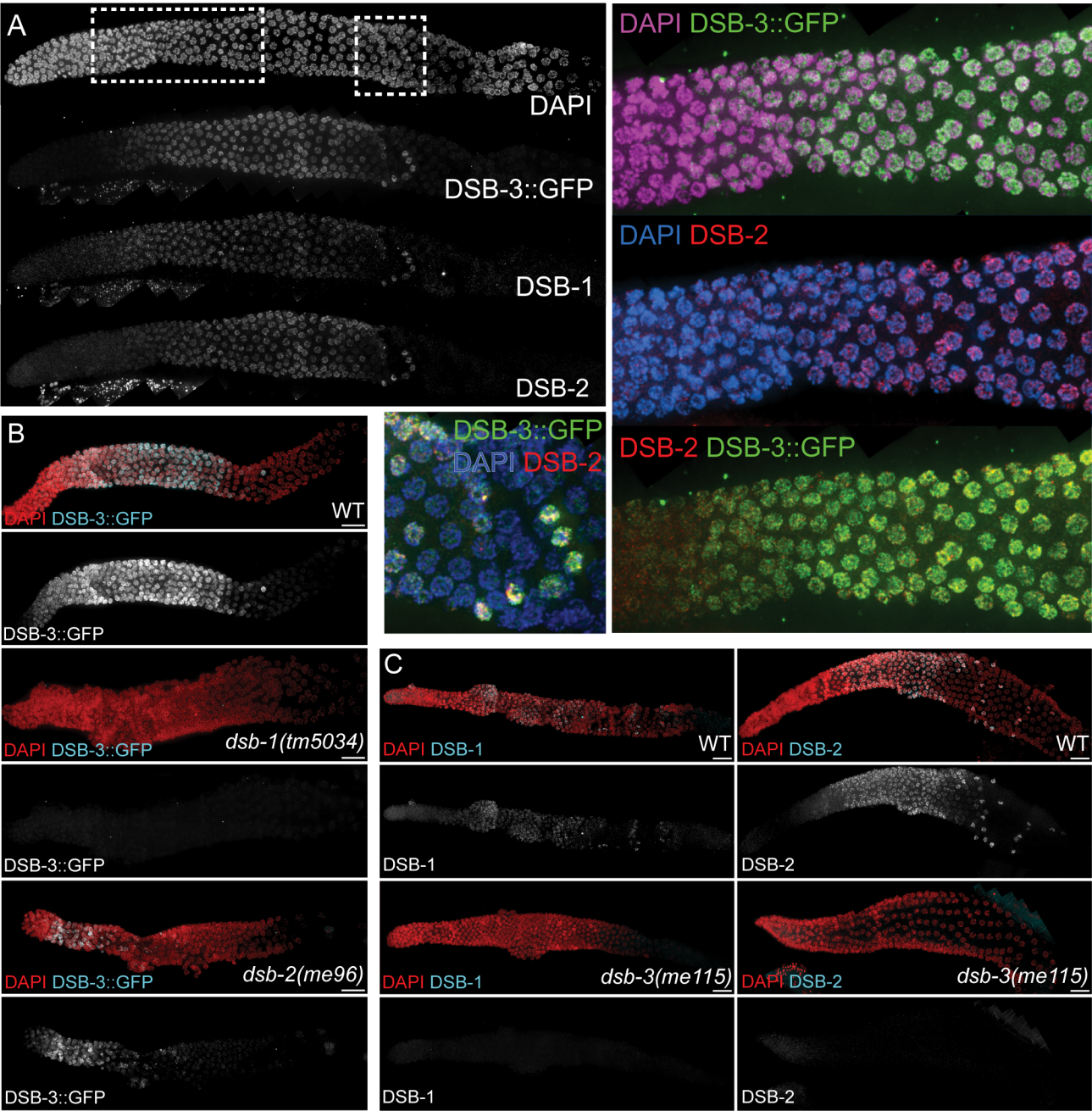
A
DAPI
DSB-3::GFP
DSB-1
DSB-2
DAPI DSB-3::GFP
DAPI DSB-2
DSB-2 DSB-3::GFP
B
DAPI DSB-3::GFP
WT
DSB-3::GFP
DSB-3::GFP
DAPI DSB-2
DAPI DSB-3::GFP
dsb-1(tm5034)
DSB-3::GFP
DAPI DSB-3::GFP
dsb-2(me96)
DSB-3::GFP
C
DAPI DSB-1
WT
DSB-1
DAPI DSB-1
dsb-3(me115)
DSB-1
DAPI DSB-2
WT
DSB-2
DAPI DSB-2
dsb-3(me115)
DSB-2

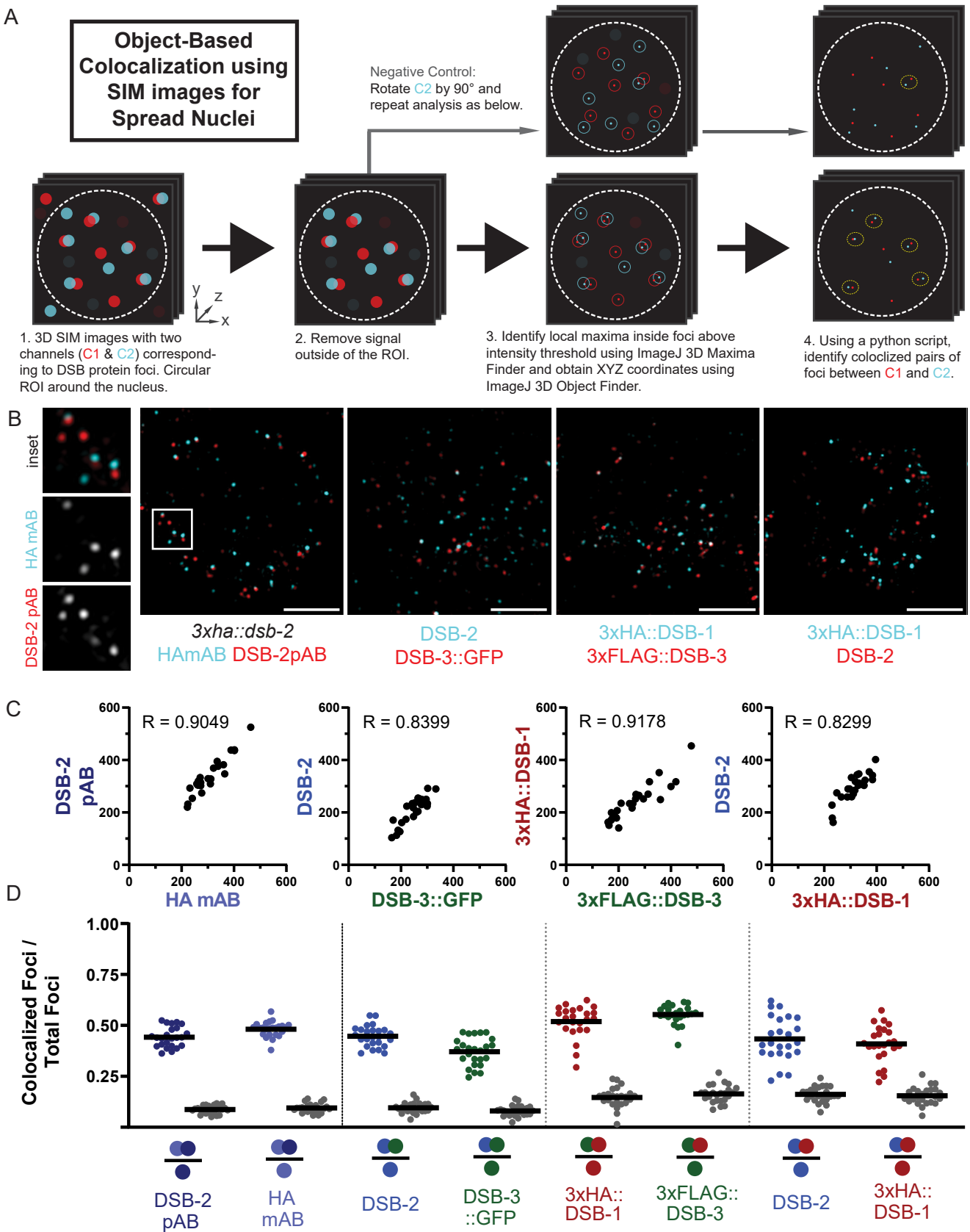
A
Object-Based Colocalization using SIM images for Spread Nuclei
Negative Control: Rotate C2 by 90° and repeat analysis as below.
y
z
x
1. 3D SIM images with two channels (C1 & C2) correspond-ing to DSB protein foci. Circular ROI around the nucleus.
2. Remove signal outside of the ROI.
3. Identify local maxima inside foci above intensity threshold using ImageJ 3D Maxima Finder and obtain XYZ coordinates using ImageJ 3D Object Finder.
4. Using a python script, identify coloclized pairs of foci between C1 and C2.
B
inset
HA mAB
DSB-2 pAB
3xha::dsb-2
HAmAB DSB-2pAB
DSB-2
DSB-3::GFP
3xHA::DSB-1
3xFLAG::DSB-3
3xHA::DSB-1
DSB-2
C
R = 0.9049
DSB-2 pAB
HA mAB
R = 0.8399
DSB-2
DSB-3::GFP
R = 0.9178
3xHA::DSB-1
3xFLAG::DSB-3
R = 0.8299
DSB-2
3xHA::DSB-1
0
200
400
600
D
Colocalized Foci / Total Foci
1.00
0.75
0.50
0.25
DSB-2 pAB
HA mAB
DSB-2
DSB-3 ::GFP
3xHA:: DSB-1
3xFLAG:: DSB-3
DSB-2
3xHA:: DSB-1

A

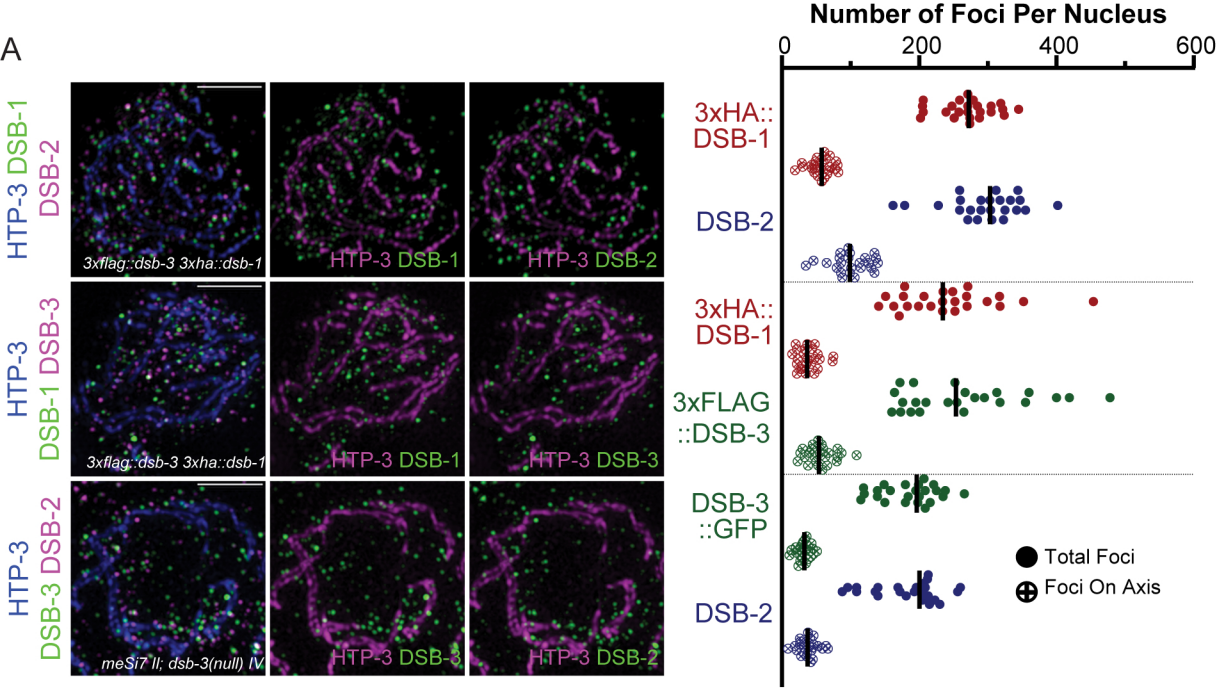
HTP-3 DSB-1 DSB-2
3xflag::dsb-3 3xha::dsb-1
HTP-3 DSB-1
HTP-3 DSB-2
HTP-3 DSB-1 DSB-3
3xflag::dsb-3 3xha::dsb-1
HTP-3 DSB-1
HTP-3 DSB-3
HTP-3 DSB-3 DSB-2
meSi7 II; dsb-3(null) IV
HTP-3 DSB-3
HTP-3 DSB-2
Number of Foci Per Nucleus
0
200
400
600
3xHA::
DSB-1
DSB-2
3xHA::
DSB-1
3xFLAG
::DSB-3
DSB-3
::GFP
DSB-2
Total Foci
Foci On Axis

B

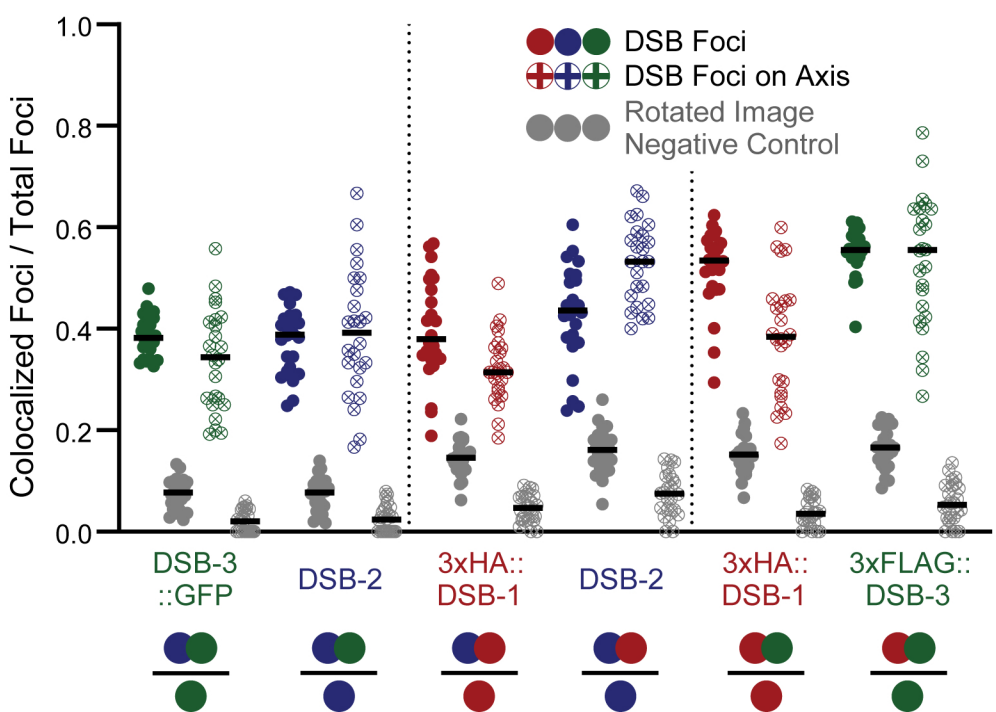
Colocalized Foci / Total Foci
1.0
0.8
0.6
0.4
0.2
0.0
DSB Foci
DSB Foci on Axis
Rotated Image
Negative Control
DSB-3
::GFP
DSB-2
3xHA::
DSB-1
DSB-2
3xHA::
DSB-1
3xFLAG::
DSB-3

A

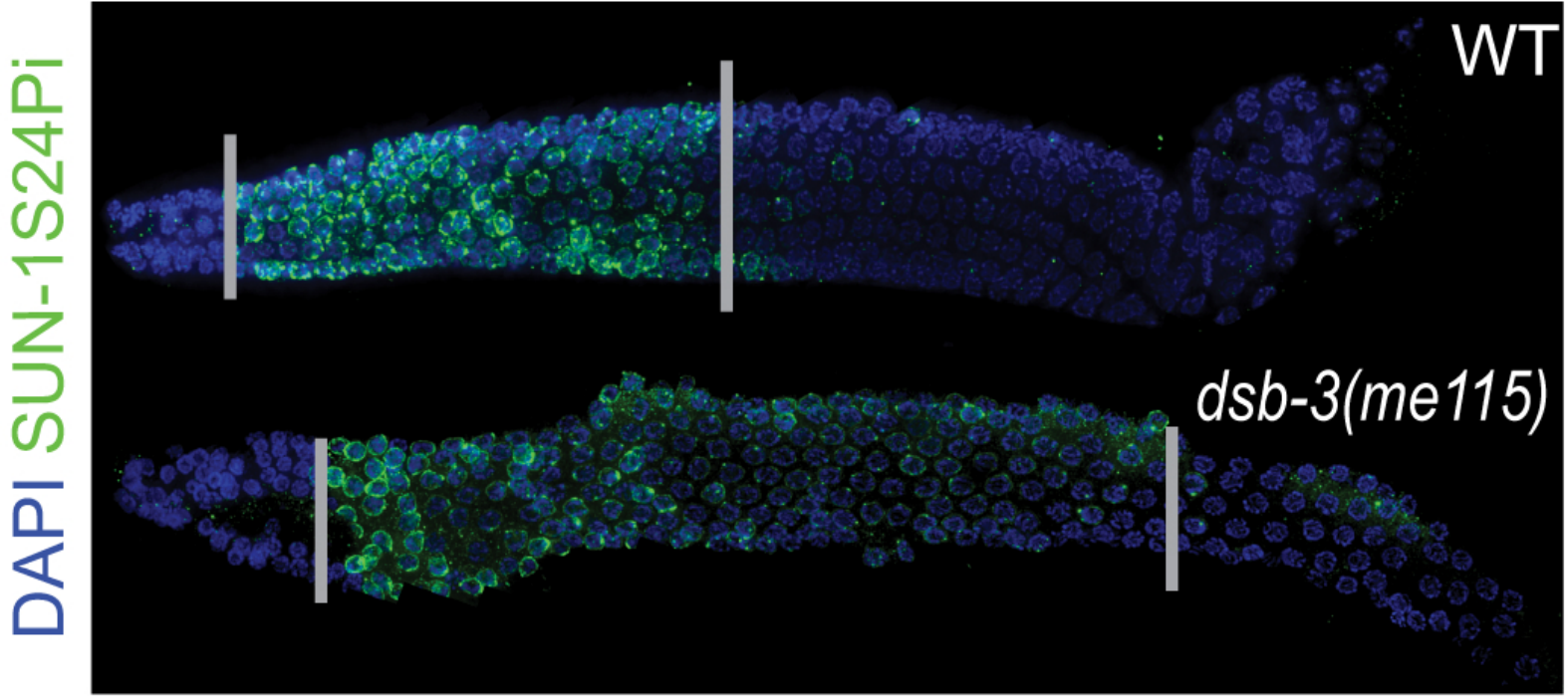
DAPI SUN-1S24Pi
WT
dsb-3(me115)

B

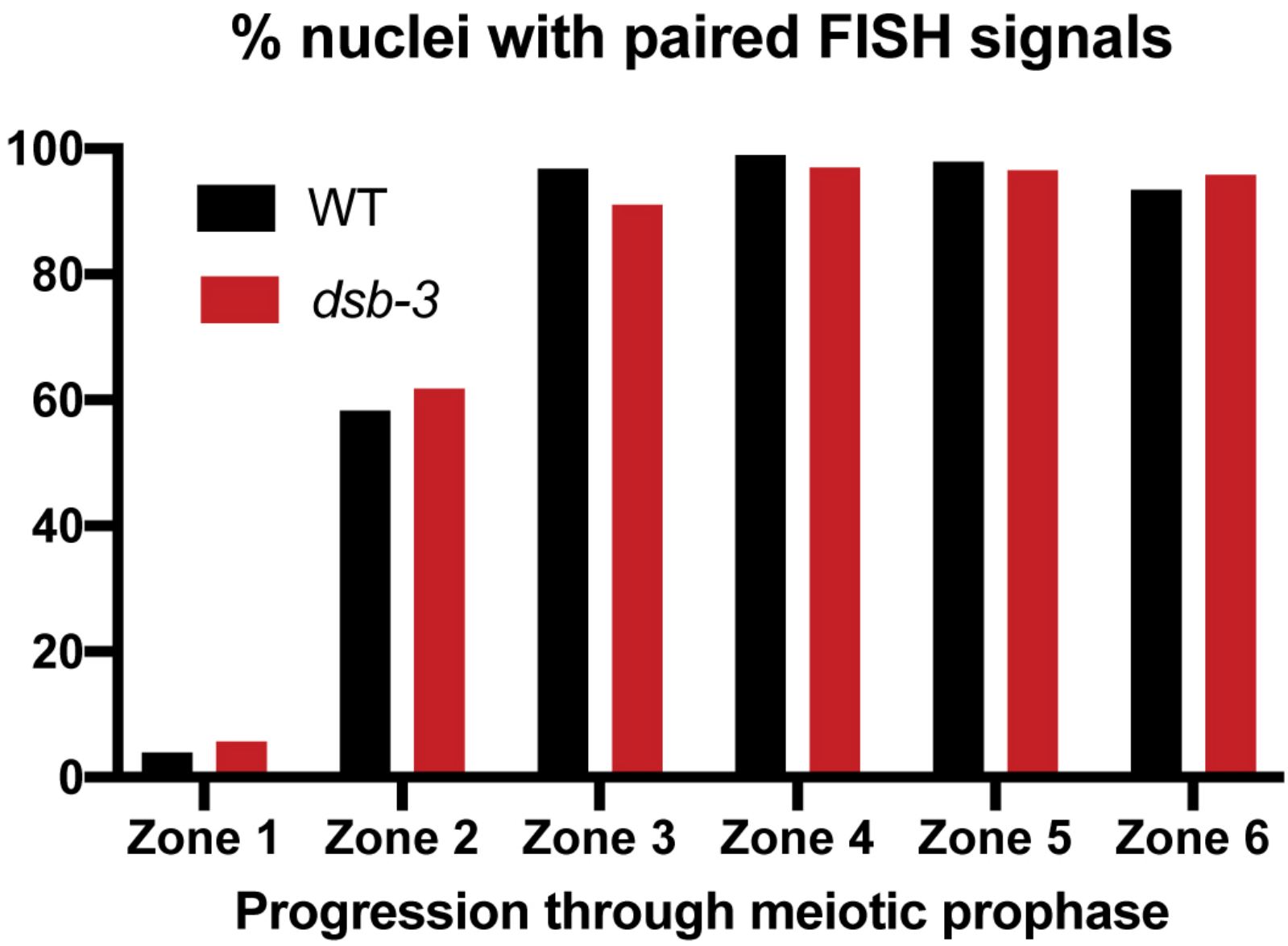
% nuclei with paired FISH signals
100
80
60
40
20
0
WT
dsb-3
Zone 1
Zone 2
Zone 3
Zone 4
Zone 5
Zone 6
Progression through meiotic prophase

A

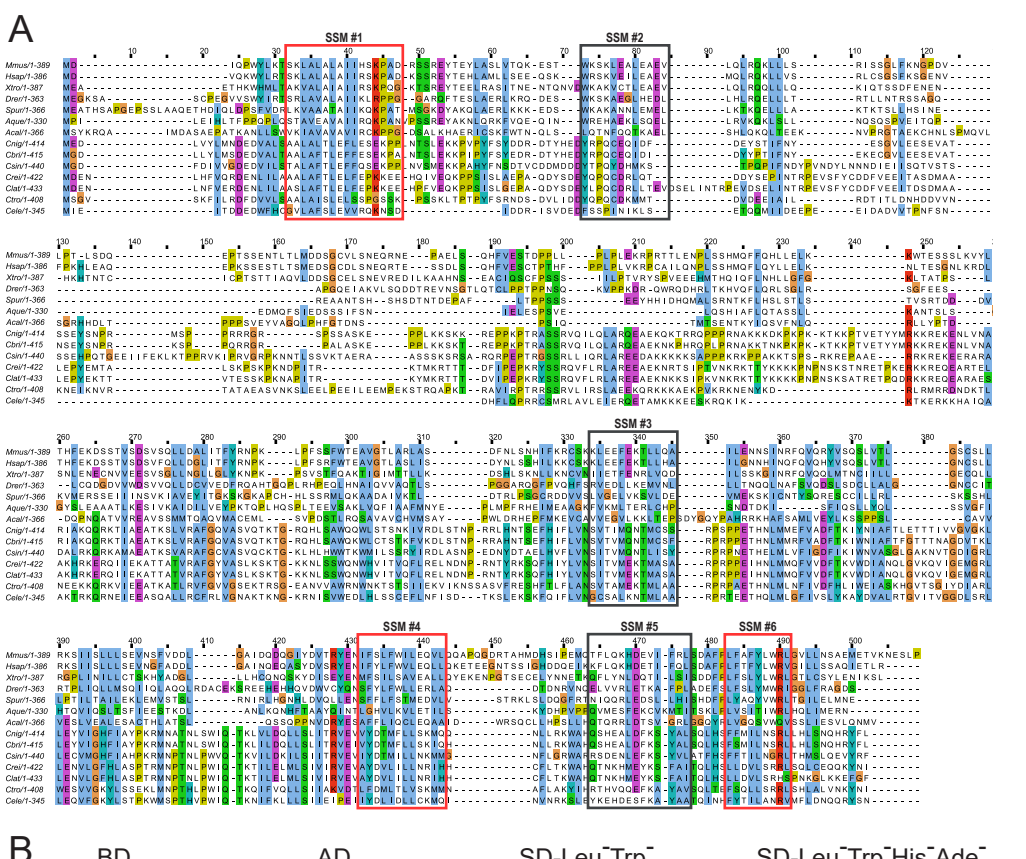

B

BD	AD
SPO-11 (Δ1-47)	AD
DSB-1	AD
DSB-2	AD
DSB-3	AD
BD	SPO-11 (Δ1-47)
BD	DSB-1
BD	DSB-2
BD	DSB-3

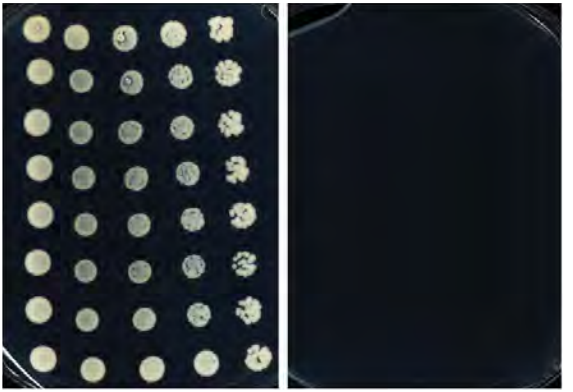

A

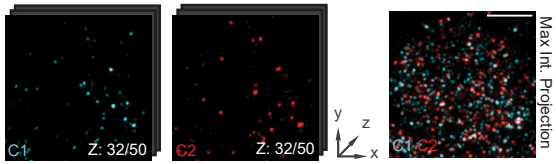

1. For each nucleus analyzed, a 3D Z-Stack SIM image, with two channels (C1 & C2) corresponding to DSB protein foci, was imported into ImageJ.

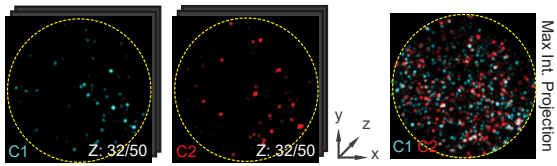

2. Circular ROI was drawn around the nucleus, signal outside of the ROI was cleared, and image was converted to 8-bit.

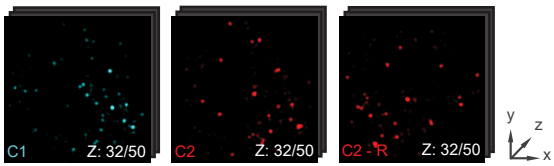

3. A duplicate C2 window was created and image was rotated by 90 degrees in XY to create a negative control image stack (C2-R) to be analyzed in conjunction with unmodified C1.

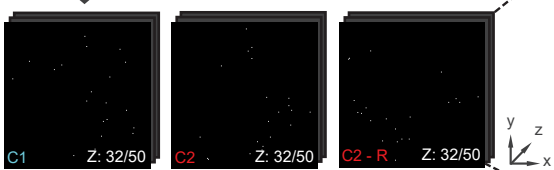

4. 3D Maxima Finder of the 3D ImageJ Suite v3.03 was used to identify local maxima within the foci in the image stack. Note in example above, the local maxima may be located in a Z-slice above or below the depicted slice.

5. 3D Object Counter v2.0 was used to extract the XYZ coordinates of the identified maxima (threshold was set to the minimum of 1 as background thresholding was addressed at a prior step). These XYZ coordinates were saved, and for each C1 focus, a custom python script was used to calculate the XY and Z distances to the nearest neighboring C2 focus (and vice versa). Negative controls distances were similarly calculated for C1 and C2-R. The script then reports the numbers and identities of C1 foci considered to be colocalized with C2 (or C2-R foci), or vice versa, based on a defined colocalization distance threshold.

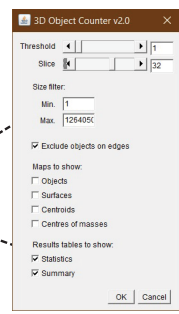

B

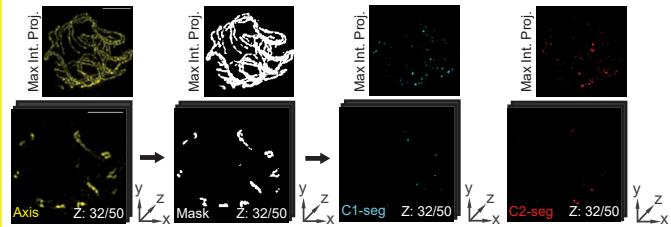

A subset of our analyses also segmented C1 or C2 signals depending on whether they coincided with a meiotic axis signal. To accomplish this, we took the 3D Z-stack of SIM images of axis fluorescence and thresholded them (ImageJ>Image>Adjust>Threshold) using the Otsu algorithm, stack histogram setting, and black background parameters enabled. We then adjusted the resulting mask for image calculations (ImageJ>Process>Math [Divide...255]), so that pixels within the mask were assigned a value of 1 and pixels outside the mask had a value of 0. We then used the image calculator to multiply each channel (C1 or C2) with the mask/background values (ImageJ>Process>Image Calculator) to identify foci that had pixels that were included within the mask..

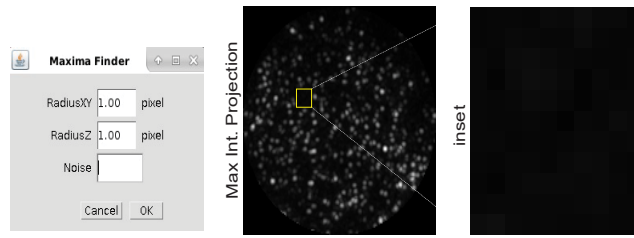

Parameters for 3D Maxima Finder: Radius XY and Radius Z were set to the minimum value of 1.00 pixel. The noise threshold was established by measuring the background fluorescence (in a maximum intensity projection) within an ROI, located inside the nucleus, that lacked any visible signal discernible as a focus. The maximum intensity measured within such an ROI was used as the noise parameter.

XY distance between C1 and C2 foci maxima

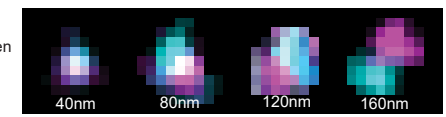

The custom python script compares the XYZ coordinates of foci detected in two channels from the output statistics of 3D Object Counter. It calculates the distances between nearest neighbor foci from these two channels and flags all combinations with a distance below a defined threshold that indicates colocalization.

In our analysis, we used 120nm as the XY distance threshold and 340nm as the Z distance threshold to indicate colocalization; these are the reported resolution limits of the DeltaVison OMX Blaze SIM microscopy system used in our study. These XY threshold values were corroborated independently through unsupervised empirical scoring or foci pairs as colocalized/not colocalized based on visual inspection of projected images (example above).

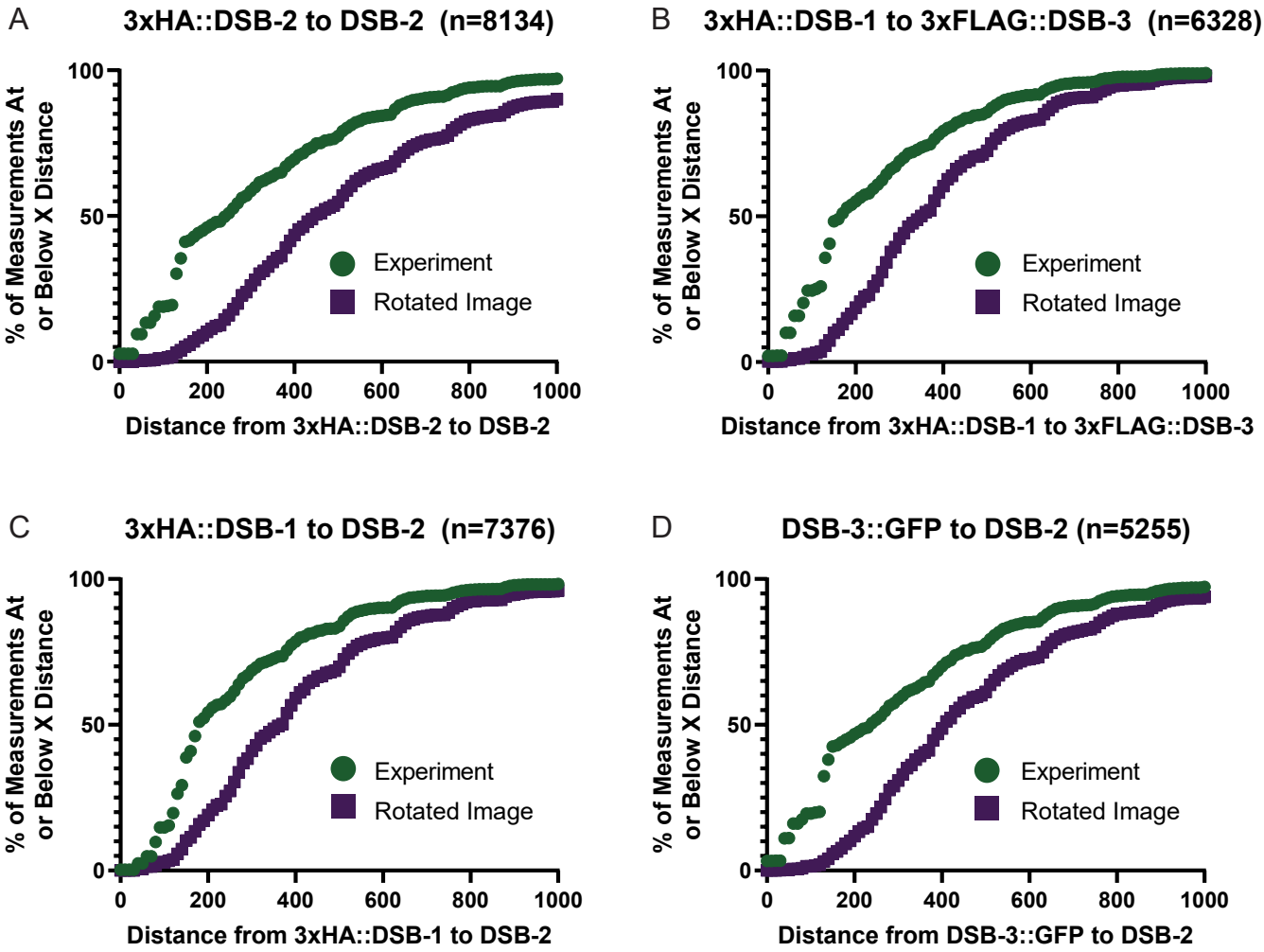
A
3xHA::DSB-2 to DSB-2 (n=8134)
% of Measurements At or Below X Distance
Distance from 3xHA::DSB-2 to DSB-2
Experiment
Rotated Image
B
3xHA::DSB-1 to 3xFLAG::DSB-3 (n=6328)
% of Measurements At or Below X Distance
Distance from 3xHA::DSB-1 to 3xFLAG::DSB-3
Experiment
Rotated Image
C
3xHA::DSB-1 to DSB-2 (n=7376)
% of Measurements At or Below X Distance
Distance from 3xHA::DSB-1 to DSB-2
Experiment
Rotated Image
D
DSB-3::GFP to DSB-2 (n=5255)
% of Measurements At or Below X Distance
Distance from DSB-3::GFP to DSB-2
Experiment
Rotated Image

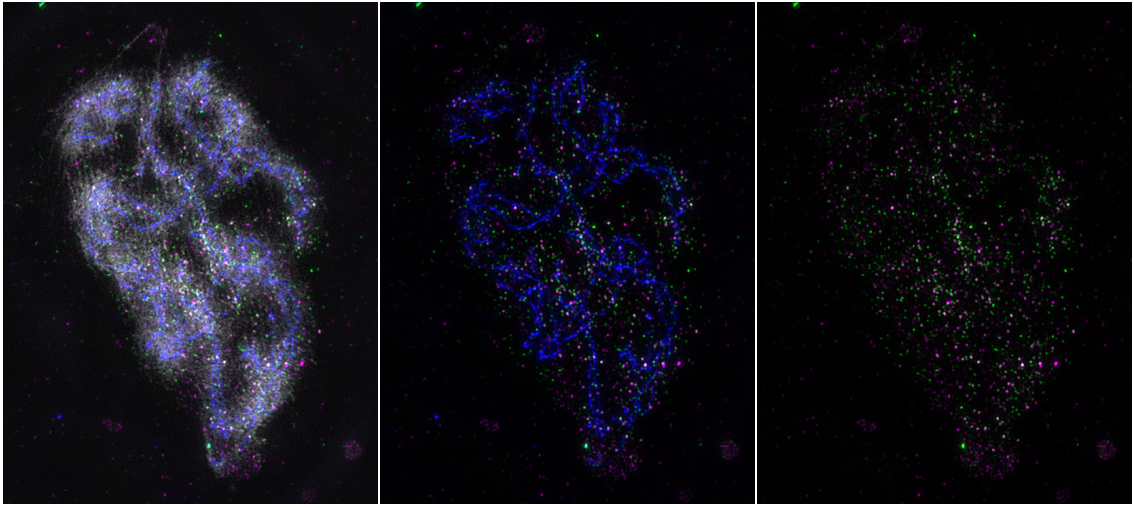
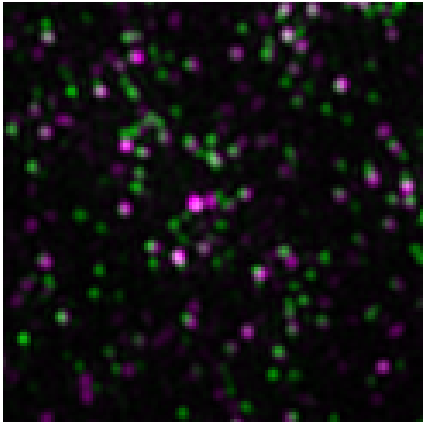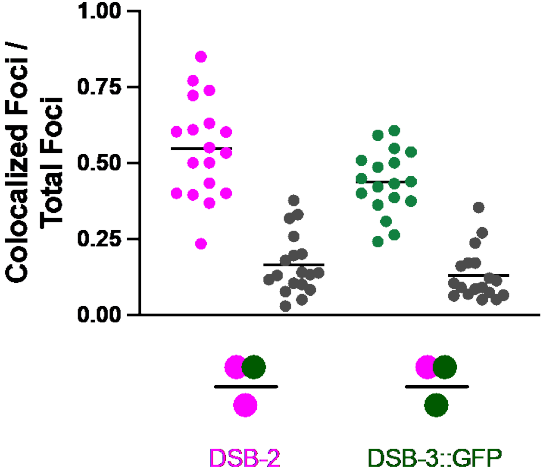
DAPI DSB-3::GFP
HTP-3 DSB-2